

**Slab temperature evolution over the lifetime of a subduction zone**

**A. F. Holt<sup>1</sup> and C. B. Condit<sup>2</sup>**

1: Rosenstiel School of Marine and Atmospheric Sciences, University of Miami, Miami, FL.

2: Department of Earth and Space Sciences, University of Washington, Seattle, WA.

Corresponding author: Adam F. Holt ([aholt@miami.edu](mailto:aholt@miami.edu))

Author ORCIDs: 0000-0002-7259-0279 (Holt), 0000-0001-7392-7681 (Condit)

Author Twitter handles: @AdamFHolt @CailCon

This manuscript has been submitted for publication in *Geochemistry, Geophysics, Geosystems*. This version has not undergone peer review and subsequent versions of this manuscript may have slightly different content. If accepted, the final version of this manuscript will be accessible via the “Peer-reviewed Publication DOI” link on the right-hand side of this webpage.

## ABSTRACT

1 The thermal evolution of subducting slabs controls a range of subduction processes, yet we lack  
2 a robust understanding of how thermal structure develops over a subduction zone's lifetime. We  
3 investigate the time-dependence of slab thermal structure using dynamically consistent, time  
4 evolving models. Pressure-temperature ( $P$ - $T$ ) conditions along the slab Moho and slab top  
5 exhibit substantial variability throughout the various phases of subduction: initiation, free  
6 sinking, mature subduction. This variability occurs in response to time-dependent subduction  
7 properties (e.g., fast vs. slow convergence) and thermal structure inherited from previous phases  
8 (e.g., due to upper plate aging). At a given depth, the slab cools rapidly during subduction  
9 initiation, after which slower cooling occurs. In the case of the Moho, additional cooling occurs  
10 during the free sinking phase. We explore the implications of time-dependent thermal structure  
11 on exhumed rocks and subducting lithosphere dehydration. Modeled slab top  $P$ - $T$  paths span  
12 much of the  $P$ - $T$  space associated with exhumed rocks, indicating that a significant component of  
13 recorded variability may have dynamic origins. Coupling our  $P$ - $T$  profiles with thermodynamic  
14 models of oceanic lithosphere, we show that dehydrating ultramafic rocks at the slab Moho  
15 provide the bulk of hydrous fluid at subarc depths during the earliest phases. Over subsequent  
16 phases, these rocks carry fluids into the deeper mantle, and it is mafic crust along the slab top  
17 that releases water at subarc depths. We conclude that rapidly varying subduction conditions, and  
18 non-steady-state thermal structure, challenge the utility of kinematically-driven models,  
19 particularly for predicting thermal structure in the geological past.

## 1. INTRODUCTION

20 The thermal structure of subduction zones enacts a first order control on a wide range subduction  
21 processes and properties, from the rheological strength of an individual plate interface to material  
22 transport, chemical transformations, and global element cycling. This thermal structure  
23 contributes to element cycling by affecting the locus and magnitude of devolatilization, and the  
24 amount of volatiles that subduct past the arc and into the deeper mantle (Hacker, 2008; Rüpke et  
25 al., 2004). Given the importance of these thermally controlled processes, a longstanding goal of  
26 subduction research is a quantitative understanding of subduction zone thermal structure.

27  
28 While analytical and semi-analytical models established the first-order controls on subduction  
29 zone temperature fields (McKenzie, 1969; 1970) and subsequently refined thermal estimates  
30 (e.g., Molnar and England, 1990; 1995; Royden, 1993; Davies, 1999), the thermal structure of  
31 subduction zones is now most commonly investigated using numerical calculations of mantle  
32 wedge flow (e.g., Furukawa, 1993; van Keken et al., 2002; Currie et al., 2004). These models  
33 typically prescribe the kinematic behavior of the subducting plate and calculate the resulting  
34 thermal solution for the mantle wedge. Use of specific subduction parameters makes such  
35 models readily applicable to individual currently active subduction zones and so, when  
36 constrained using geophysical or petrological observables, they have led to important insights  
37 about Earth's down-going water flux (Syracuse et al., 2010; van Keken et al., 2011), drivers of  
38 arc magmatism (e.g., Grove et al., 2009; Perrin et al., 2018), and exhumation potential of  
39 subduction zone rocks (Gerya et al., 2002; van Keken et al., 2018). In such models, subduction  
40 zone thermal structure is predicted by either holding subduction properties constant to derive a  
41 steady-state solution, as in most of the studies mentioned above, or by imposing time-varying  
42 slab properties within models (e.g., Peacock and Wang, 1999; Hall, 2002; Suenaga et al., 2019).  
43 However, because these approaches impose slab and plate properties, they are unable to  
44 investigate the time-dependence of subduction zone thermal structure (and associated non-steady  
45 state effects) within a framework that permits the slab, plates, and mantle wedge to co-evolve in  
46 a dynamically consistent manner.

47  
48 Tectonic and plate kinematic observations demonstrate that the properties governing slab  
49 temperatures, such as slab dip, convergence rate, and upper plate structure, can vary over few-  
50 Myr timescales (e.g., Faccenna et al., 2001; Sdrolias and Müller et al., 2006; Iaffaldano, 2015).  
51 Such observations are supported by similarly fast subduction zone variation in dynamic  
52 subduction models (Clark et al., 2008; Cerpa et al., 2014), with models exhibiting distinct phases  
53 throughout the lifetime of a subduction zone that can last for several Myrs and are characterized  
54 by differing plate motions, trench motions, and/or slab dips (e.g., Funiciello et al., 2004; Garel et  
55 al., 2014; Holt et al., 2015). Given this inherent subduction zone time dependence, and the links  
56 between subduction properties and thermal structure, it is then unsurprising that time-dependent  
57 pressure-temperature ( $P$ - $T$ ) conditions are recorded in the metamorphic rocks exhumed at a wide

58 range of paleo subduction zones (e.g., Lázaro et al., 2009; Groppo et al., 2009; Krebs et al.,  
59 2011).

60

61 Motivated by this, we use time-dependent and self-consistently evolving numerical models to  
62 investigate the imprint that dynamic changes in subduction behavior have on slab Moho and slab  
63 top temperature. For convenience, we refer to our models as ‘*dynamic*’ and the more common  
64 mantle wedge models that prescribe slab and overriding plate properties as either ‘*kinematic-*  
65 *dynamic*’ or ‘*kinematically-driven*’ models. That is, the latter set of models kinematically  
66 prescribe the slab and upper plate behavior but derive a dynamic solution for flow and thermal  
67 structure in the mantle wedge. We note that some thermal subduction models fall between these  
68 endmembers, e.g., models that include flow in the wedge that is driven by compositional density  
69 anomalies (e.g., Gerya et al., 2002; Gerya and Yuen, 2003) or prescribe plate velocities but solve  
70 for slab evolution and/or upper plate deformation (e.g., Eberle et al., 2002; Yamato et al., 2007;  
71 Arcay, 2012; 2017). However, only a very limited set of studies have examined the evolution of  
72 slab pressure-temperature (*P-T*) conditions within models that do not impose any external forces  
73 or velocities on the flow (King and Ita, 1995; Kincaid and Sacks, 1997). While dynamic models  
74 are challenging to tailor to specific subduction zones, they allow us to develop intuition about  
75 non-steady-state thermal structure in a generalized sense. At the scale of an individual  
76 subduction zone, such an understanding is needed to move towards: i) accounting for thermal  
77 structure that has been inherited from previous phases in present day thermal structure estimates,  
78 ii) assessing how rapidly thermal structure varies, and iii) constraining how temperature-  
79 dependent observables may vary within the geological record.

80

81 Temporal changes in subduction zone thermal structure can be expected to manifest in a range of  
82 geological phenomena. After fingerprinting the various phases of subduction zone thermal  
83 structure, we also use our models to assess the relations of slab temperature variations on two  
84 phenomena: *P-T* conditions recorded in exhumed rocks, and dehydration depths and magnitudes  
85 within the downgoing lithosphere. The exhumed rock record reflects subduction zone  
86 temperatures that are, in general, warmer than the equivalent temperatures in modeled  
87 subduction zones by a few hundred degrees (Guillot et al., 2009; Penniston-Dorland et al. 2015;  
88 Gerya et al., 2002; Syracuse et al., 2010). In addition to a potential contribution from additional  
89 heat sources, including shear heating which can increase slab top temperatures most substantially  
90 at depths undergoing frictional deformation  $< \sim 50$  km (e.g., Peacock, 1992; Gao and Wang,  
91 2014; Penniston-Dorland et al. 2015), preferential exhumation of subduction terranes at young  
92 subduction zones and/or during the warmer early stages of subduction offer alternative  
93 explanations for this temperature discrepancy (Agard et al., 2009; Abers et al., 2017; van Keken  
94 et al., 2018).

95

96 Our models enable us to develop a dynamically consistent basis for the thermal cooling that  
97 occurs during subduction initiation, and to identify more subtle thermal phases that occur later  
98 on. We find that the resulting time-dependence of crustal temperature is, in a single model

99 subduction zone, significant enough to cover much of the  $P$ - $T$  space recorded by exhumed rocks.  
 100 For subduction zone models with a range of mechanical parameters (slab strength, crust viscosity  
 101 and rheology, lower mantle viscosity), slab tops undergo rapid cooling during subduction  
 102 initiation followed by cooling at a reduced rate during the latter phases. The slab Moho  
 103 undergoes a similar thermal evolution but with the addition of a 5 to 10 Myr long cooling  
 104 transient that occurs as the slab sinks rapidly through the relatively weak upper mantle. When  
 105 such  $P$ - $T$  conditions are coupled with thermodynamic models of oceanic crust and mantle  
 106 dehydration, they suggest strong temporal variability in the degree and location of oceanic  
 107 lithosphere dehydration throughout the lifetime of a subduction zone. Fluid sources within the  
 108 subarc mantle are likely from dehydration of ultramafic rocks along the slab Moho during the  
 109 warmest early stages of subduction, and switch to fluids sourced from subducting oceanic crust  
 110 as the subduction zone matures. In these later, colder stages of subduction, hydrated oceanic  
 111 mantle will carry mineral-bound  $H_2O$  well past the subarc into the deeper mantle (e.g., Rüpke et  
 112 al., 2004; Hacker et al., 2008; van Keken et al., 2011). These evolving thermal structures clearly  
 113 have important implications for fluid sources, global element cycling, and recorded  $P$ - $T$   
 114 conditions of exhumed subduction-related terranes.

115

## 116 **2. METHOD**

117

### 118 **2.1. Modeling overview**

119

120 We use the ASPECT code (version 2.1.0) to construct numerical, time-evolving subduction  
 121 models within 2-D domains (Kronbichler et al., 2012; Heister et al., 2017; Bangerth et al., 2020a;  
 122 2020b). ASPECT was used to solve the conservation equations that govern convection in an  
 123 incompressible viscous fluid (Boussinesq approximation) with negligible inertia: the  
 124 conservation of energy (no internal heating), mass (continuity equation), momentum (Stokes  
 125 equation), and the advection of compositional fields (e.g., for the weak crust of the subducting  
 126 plate). The models evolve dynamically in that there are no external forces or velocities applied to  
 127 the subduction system. In this section, we describe the geometrical, mechanical, and rheological  
 128 properties of our subduction models, with a focus on our reference model (Figs. 1-4). Table 1  
 129 provides the parameter values of this reference model.

130

131 Subduction is modeled within a whole mantle domain (2900 x 11600 km), where all boundaries  
 132 are mechanically free slip. We begin our models with two flat laying thermal plates. A 90 Ma,  
 133 6000 km long plate is placed next to a 10 Ma, 2500 km long plate and the two plates are  
 134 separated by a weak crustal layer (Fig. 1a). The older and denser plate bends and subducts  
 135 beneath the younger plate in a style broadly analogous to subduction initiation at a transform  
 136 fault (e.g., Matsumoto and Tomada, 1983).

137

138

139

## 140 2.2. Thermal structure

141

142 The initially flat lying lithospheric plates are defined by half space cooling profiles  
 143 corresponding to ages of 90 and 10 Ma, a thermal diffusivity of  $10^{-6}$  m<sup>2</sup>/s, and a 1421.5 °C  
 144 mantle potential temperature equivalent to that of the GDH1 plate cooling model (Stein and  
 145 Stein, 1992). Constant temperatures are imposed at the model boundaries (0 °C surface, 1421.5  
 146 °C base and sides). We assume incompressibility in our models and add a 0.3 °C/km adiabatic  
 147 temperature gradient to our modeled temperatures as a post-processing step (e.g., van Keken et  
 148 al., 2011). Densities are purely temperature dependent and calculated relative to a reference  
 149 mantle density of 3300 kg/m<sup>3</sup> using a thermal expansion coefficient of  $3 \times 10^{-5}$  K<sup>-1</sup>.

150

## 151 2.3. Rheology

152

153 We consider a composite mantle rheology with diffusion creep, dislocation creep, and plastic  
 154 yielding components. The inclusion of stress-dependent flow (dislocation creep) in the thermal  
 155 models is important as it elevates slab top temperature (van Keken et al., 2002) and sharpens the  
 156 down-dip transition from cold to hot forearc material (Wada et al., 2011). In the modeled upper  
 157 mantle, we use idealized dislocation and diffusion creep flow laws:

158

$$159 \eta_{diff/disl} = A \frac{-1}{n} \dot{\epsilon}^{\frac{1-n}{n}} \exp\left(\frac{E+PV}{nRT}\right) \quad (1)$$

160

161 where  $A$  is a pre-factor,  $\dot{\epsilon}$  is the second invariant of the strain rate tensor,  $n$  is the stress exponent  
 162 (diffusion creep = 1, dislocation creep = 3.5),  $R$  is the gas constant,  $P$  is lithostatic pressure, and  
 163  $T$  is model temperature (including the prescribed adiabatic gradient). The activation volumes ( $V$ )  
 164 and energies ( $E$ ) are consistent with the range of experimental values determined for dry olivine  
 165 (Table 1) (e.g., Karato and Wu, 1993; Hirth and Kohlstedt, 2003). Dislocation and diffusion  
 166 creep pre-factors are set to give  $\eta_{diff} = \eta_{disl} = 5 \times 10^{20}$  Pa s at a depth of 330 km and strain  
 167 rate of  $5 \times 10^{-15}$  s<sup>-1</sup>. This produces a reference upper mantle viscosity of  $2.5 \times 10^{20}$  Pa s (Eq. 4)  
 168 and dislocation creep deformation adjacent to rapidly moving plates and slabs. Dislocation creep  
 169 occurs to average depths of about 250 km (Fig. 1b), consistent with the  $\sim 100$ –400 km inferred  
 170 from seismic anisotropy studies (e.g., Podolefsky et al. 2004; Becker, 2006). Our lower mantle is  
 171 more viscous than the upper mantle and deforms via diffusion creep only. The lower mantle  
 172 diffusion creep pre-factor is calculated to give a lower mantle diffusion creep viscosity 15 times  
 173 that of the upper mantle diffusion creep viscosity. Due to upper mantle dislocation creep, the  
 174 effective upper-to-lower mantle viscosity contrast is actually  $\approx 30$ , in broad agreement with  
 175 geoid constraints (e.g., Hager, 1984).

176

177 We also incorporate a pseudo-plastic component into our effective viscosity, which approximates  
 178 brittle yielding at lithospheric depths. The plastic viscosity,  $\eta_{yield}$ , is computed as:

179

180 
$$\eta_{yield} = \frac{\min(\tau_{yield}, 0.5 \text{ GPa})}{2\dot{\epsilon}} \quad (2)$$

181

182 Where  $\tau_{yield}$  is a Byerlee type yield stress (Byerlee, 1978):

183

184 
$$\tau_{yield} = (aP + b)\lambda \quad (3)$$

185

186  $a$  is the friction coefficient (0.6),  $b$  is cohesion (60 MPa),  $P$  is lithostatic pressure, and  $\lambda$  is a  
 187 constant ‘pore pressure’ factor (0.1), with values comparable to previous subduction modeling  
 188 studies (e.g., Enns et al., 2005). An effective model viscosity is calculated as:

189

190 
$$\eta = \left( \frac{1}{\eta_{diff}} + \frac{1}{\eta_{disl}} + \frac{1}{\eta_{yield}} \right)^{-1} \quad (4)$$

191

192 We use compositional fields to track the location of three regions that are rheologically-distinct  
 193 from the background material (the slab crust, a strong lithospheric core, and weak regions at the  
 194 edges of lithospheric plates), with each composition ( $c_i$ ) advected following:

195

196 
$$\frac{\partial c_i}{\partial t} + \mathbf{u} \cdot \nabla c_i = 0 \quad (5)$$

197

198 where  $\mathbf{u}$  is model velocity. Weak regions at the edges of the subducting and upper plates are  
 199 imposed to ensure the initiation of spreading ridges at the start of the model run. These regions  
 200 are square (75 km<sup>2</sup> in size) and have a reduced yield stress ( $\lambda = 0.025$ ). Yielding is switched off  
 201 within both the overriding plate and a 15 km thick layer in the core of the subducting plate. This  
 202 is consistent with the presence of a strong core sandwiched between a brittle-yielding upper and  
 203 ductile-yielding lower lithosphere (e.g., Karato and Wu, 1993). The final compositional field  
 204 corresponds to the weak crust which, as discussed in detail in Section 2.4, is prescribed a  
 205 constant viscosity. Each compositional field has an equivalent density to the background material  
 206 (at a given temperature).

207

208 The overall model viscosity is capped by upper and lower limits of  $2.5 \times 10^{23}$  Pa s and  $2.5$   
 209  $\times 10^{18}$  Pa s. Due to the strong temperature dependence of the flow laws (Eq. 1), the upper limit  
 210 sets the strength of our slabs in regions other than where the slab bends and yields. Hence the  
 211 non-deforming portions of our slabs are  $\sim 1000$  times stronger than the surrounding  
 212 asthenosphere. The yielding region is  $\sim 100$  times stronger. Taken together, this produces  
 213 average slab strengths compatible with the viscosity contrasts of 100 – 1000 generally required  
 214 to satisfy plate bending constraints and produce Earth-like trench motions (e.g., Wu et al., 2008;  
 215 Funicello et al., 2008).

216

217

218

**2.4. Decoupling**

219  
220  
221 In addition to enabling plate convergence, the weak crust is needed to decouple the slab from the  
222 overriding mantle wedge at depths less than about 80 km, and hence generate a cold mantle  
223 wedge corner. Low surface heat flow values and petrologically inferred low mantle temperatures  
224 at forearcs provide evidence for the occurrence of such a cold mantle wedge corner (Honda,  
225 1985; Furukawa, 1993). In our reference model, the weak crust is initially 10 km thick, imposed  
226 with an initially curved geometry (radius of curvature = 250 km), and has a viscosity of  $2 \times 10^{20}$   
227 Pa s, consistent with the experimentally determined basaltic crust viscosities at these conditions  
228 (Agard et al., 2016; Behr and Becker, 2018).

229  
230 By changing the viscosity of the crust in the down-dip direction, or simply cutting the weak  
231 crustal layer off, a transition from decoupling at shallow depths (i.e., slab is weaker than  
232 overriding wedge corner) to coupling at greater depths (slab stronger than overriding wedge)  
233 produces the cold mantle wedge corner region (e.g., Wada et al., 2008; Wada and Wang, 2009).  
234 The depth of this transition is often called the “decoupling depth” (DD) and appears to occur  
235 across most Earth subduction zones at  $\sim 80$  km (Wada and Wang, 2009). Because the DD exerts  
236 significant control on slab temperatures (Syracuse et al., 2010; Maunder et al., 2019), we  
237 examine three different decoupling parameterizations: shallow crust cut-off, deep crust cut-off,  
238 and a visco-plastic crust. In the first two cases, we cut off an isoviscous crust at a specified  
239 depth. In the shallow crust case, this cut-off depth is 80 km. In the deep crust case, this cut-off  
240 depth is 200 km. Note that this cut-off depth is not necessarily the DD but rather the maximum  
241 depth of decoupling (MDD) (cf. Wada and Wang, 2009). This is because the crust can be  
242 stronger than the overlying material at depths shallower than the MDD if the overlying wedge is  
243 hot and weak, as is the case during most of our modeled subduction. For our reference model, we  
244 choose the shallow crust cut-off case following suggestions that MDDs of 70-90 km are  
245 required to satisfy surface heat flow measurements (Furukawa, 1993; Wada and Wang, 2009),  
246 and also to render our models comparable to kinematically-driven models that choose a similar  
247 depth (e.g., Syracuse et al., 2010; van Keken et al., 2011).

248  
249 We also test the effect of assigning a stress-dependent rheology to the crust (e.g., Arcay et al.,  
250 2007; Arcay, 2012; 2017; Maunder et al., 2018). A visco-plastic rheology is prescribed in the  
251 crust with a reduced yield stress pre-factor of  $\lambda = 0.02$  (Eq. 3). As shown by Maunder et al.  
252 (2018), this enables decoupling to emerge without the need to prescribe a cut-off depth. In our  
253 models, a yield stress less than or equal to 30% of the surrounding material, which has  $\lambda = 0.1$ ,  
254 is sufficient to weaken the segment of crust between the slab and cold wedge corner. We then  
255 limit the viscosity using a lower bound that defines the yielded crustal viscosity to be equivalent  
256 to that of the isoviscous crust ( $2 \times 10^{20}$  Pa s). Without this lower bound, the yielded portion of  
257 crust becomes very weak which produces unrealistically high convergence rates ( $> 20$  cm/yr).

258  
259



## 260 2.5. Numerical parameters

261  
262 Adaptive mesh refinement (AMR) is set to occur for finite elements with large gradients in  
263 viscosity, temperature, and composition (Fig. 1c, S1). This enables us to highly resolve our 10  
264 km thick crustal layer material while also capturing flow at the scale of the whole mantle. In  
265 addition to the crust, we also highly refine the mesh within the slab core (as is also defined by a  
266 compositional field). The AMR parameters in our reference model produce a maximum level of  
267 refinement corresponding to 1.4 km wide finite element dimensions (in the crustal layer), and a  
268 minimum level of refinement corresponding to 180 km finite elements (in the lowermost  
269 mantle). Increasing the maximum resolution to the 0.7 km level does not change model  
270 temperature systematics but causes subduction to initiate slightly earlier, by about 0.5 Myr (Figs.  
271 S2, S3). We have also conducted numerical accuracy tests to ensure that our linear and nonlinear  
272 solver tolerances are sufficiently strict (Fig. S4).

## 273 274 2.6. Model analysis

275  
276 We focus our analysis on the temperatures of the upper (slab top) and lower (slab Moho)  
277 surfaces of the subducting crust. To find the location of these two profiles, we first interpolate  
278 the compositional field ( $0 < C < 1$ ) that corresponds to the crust across the model domain using a  
279 cubic interpolation scheme. We then extract pressure and temperature profiles along a contour of  
280  $C = 0.5$ , with contours on either side of the layer corresponding to the slab top and slab Moho.  
281 To correct for roughness in the slab top  $P$ - $T$  profiles, we smooth the profiles using a Savitzky-  
282 Golay filter (cf. Figs. 3 and S5 for smoothed vs. raw profiles). This roughness occurs due to a  
283 combination of the strong thermal gradient between the cold slab and hot wedge and our use of  
284 rectangular finite elements (i.e., which are not angled along the slab top). However, this  
285 roughness (perturbations of  $< \sim 10$  °C) is minor relative to the temperature variability between  
286 analyzed timesteps ( $\sim 50$  °C) (Fig. S5). Our resolution tests confirm that further increases in the  
287 mesh resolution have minimal effect on the overall  $P$ - $T$  evolution (Fig. S3). For the dehydration  
288 calculations, described next, we take the additional step of interpolating our  $P$ - $T$  profiles using  
289 modeled convergence rates (Fig. 2a). This enables us to capture the time evolution of slab  
290 temperature that occurs as a hypothetical rock package descends down the subduction zone.

291  
292 We next couple these interpolated  $P$ - $T$  profiles of the slab top and slab Moho to thermodynamic  
293 models of oceanic crust (average Mid Ocean Ridge Basalt [MORB]), and depleted MORB  
294 mantle (DMM) to demonstrate how dehydration depths and magnitudes can vary between these  
295 two portions of the subducting slab as slab thermal structure evolves. We focus on oceanic  
296 lithosphere rather than other lithologies because it has been shown to be the major fluid source in  
297 most subduction systems (Schmidt and Poli, 1998; Rüpke et al., 2004; Hacker, 2008; Hernández-  
298 Uribe and Palin, 2019; Condit et al., 2020). Our thermodynamic models were made using the  
299 software *Perple\_X* 6.8.3 (Connolly and Pettrini, 2002), and use the same solution models and  
300 approach as Condit et al. (2020). Details of these models including the bulk compositions used,

301 chemical system, thermodynamic datasets, solution phase models and equations of state are  
 302 provided in Tables S1 and S2. Our models encompass  $P$ - $T$  conditions ranging from 0.1 to 4.5  
 303 GPa and 200 to 750°C (Fig. S6). For simplicity, we assume MORB and DMM are both H<sub>2</sub>O  
 304 saturated, which is an apt assumption for the fluid-rich plate interface (e.g., Jarrard, 2003;  
 305 Bebout& Penniston-Dorland, 2016) and discrete fractures and bending fault zones in mantle  
 306 lithosphere (e.g., Peacock, 2001; Naif et al., 2015, Grevemeyer et al., 2018). We treat fluids as  
 307 pure H<sub>2</sub>O. Along each of the interpolated slab top and slab Moho  $P$ - $T$  paths, we extract the  
 308 mineral-bound H<sub>2</sub>O remaining in each lithology as they subduct. Together, we use these results  
 309 to investigate the first order relationship between the evolving thermal structure and patterns of  
 310 metamorphic H<sub>2</sub>O loss over the lifetime of a subduction zone.

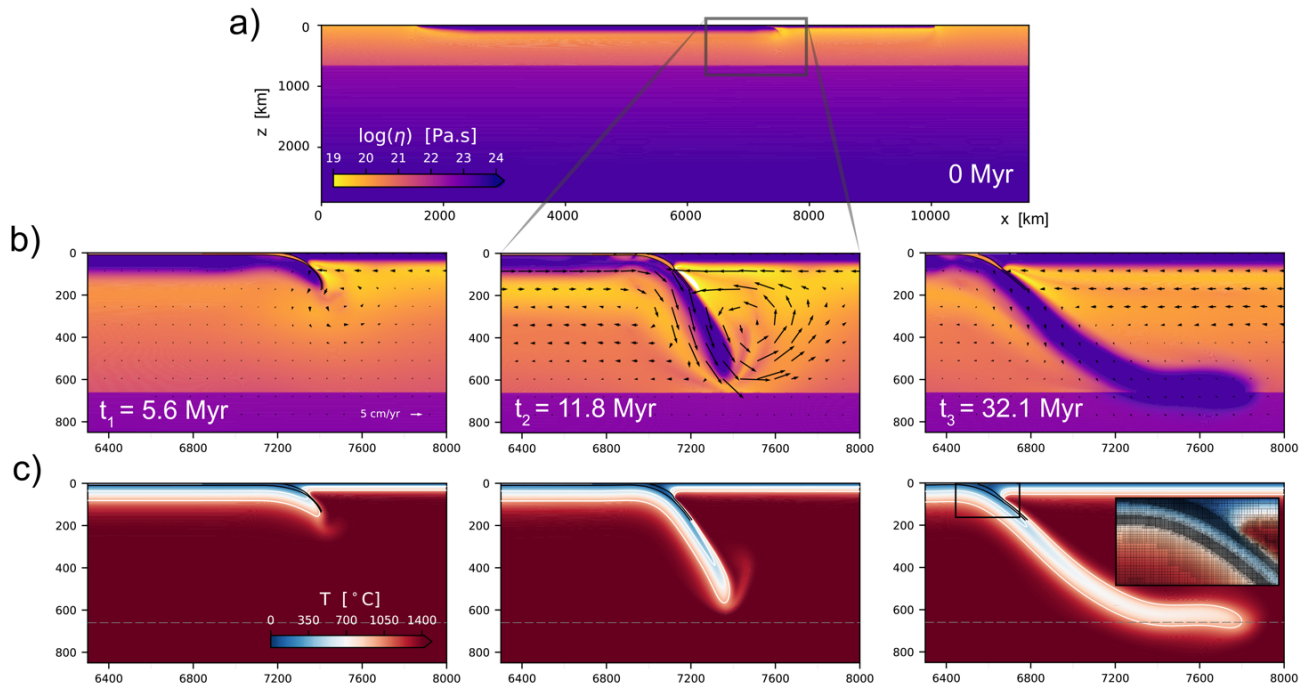


**Figure 1:** Evolution of the reference model. Panels show: A) the initial viscosity field of the entire model domain, B) evolution of the viscosity and velocity fields zoomed into a region around the subduction zone, C) the temperature field evolution. Three time-steps shown correspond to the initiation ( $t_1 = 5.6$  Myr), free sinking ( $t_2 = 11.8$  Myr), and mature phases ( $t_3 = 32.1$  Myr). Isotherms (500°C, 1000°C) and the boundaries of the compositional crust are overlain on C. A zoom-in of the computational mesh is overlain on the mature phase of C (note the highly refined crust and slab core regions).

### 311 3. RESULTS

312

#### 313 3.1. Geodynamic evolution

314

315 We begin by describing the evolution of our reference model (see Table S1 for parameters).

316 Over approximately 8 Myr, the originally flat-lying subducting plate initiates into a slab, aided  
 317 by plastic yielding and the initial positioning of the weak crustal channel. At a model time of 5.6  
 318 Myr, during this “initiation phase”, the proto-slab has subducted to a depth of 160 km (Fig. 1)

319 and the convergence rate of the system is  $\approx 3$  cm/yr (Fig. 2a). The subducting plate is  
 320 approximately stationary and so this convergence rate is a result of trench retreat ( $v_T$ ) at  $\approx 3$   
 321 cm/yr. Subduction initiation over 8 Myr is sluggish but in broad agreement with a selection of  
 322 independent geological (Agard et al., 2020) and numerical estimates (Dymkova and Gerya,  
 323 2013).

324

325 As the slab subducts deeper, and the total negative buoyancy increases, the convergence rate  
 326 increases during the “free-sinking phase” (i.e., slab sinking through the upper mantle).  
 327 Convergence rates are maximum during this phase as the excess bending resistance to  
 328 subduction initiation has been overcome, while slab has not yet reached the high viscosity lower  
 329 mantle. As seen in previous models (e.g., Holt and Becker, 2017), this pulse of rapid plate  
 330 convergence is enhanced by a reduction in viscous resistance in the upper mantle that occurs due  
 331 to wide-spread activation of dislocation creep (Figs. 1b, 2a). Our second snapshot is at a model  
 332 time of 11.8 Myr, where the  $\approx 12$  cm/yr convergence rate is near the model’s maximum value  
 333 and the slab dip is  $51^\circ$  at shallow depths (125 km depth). The 12 cm/yr convergence rate is  
 334 partitioned between a subducting plate velocity ( $v_{SP}$ ) of  $\approx 7$  cm/yr and  $v_T$  of  $\approx 5$  cm/yr. The  
 335 initially uniformly thick (10 km) crust gradually thickens to  $\approx 15$  km as it descends into the  
 336 trench. This is because slab rollback induces horizontal extension in the crust at upper plate  
 337 depths which, in turn, thickens it locally within this region (cf., Holt et al., 2017; Sandiford and  
 338 Moresi, 2019; Beall et al., 2020).

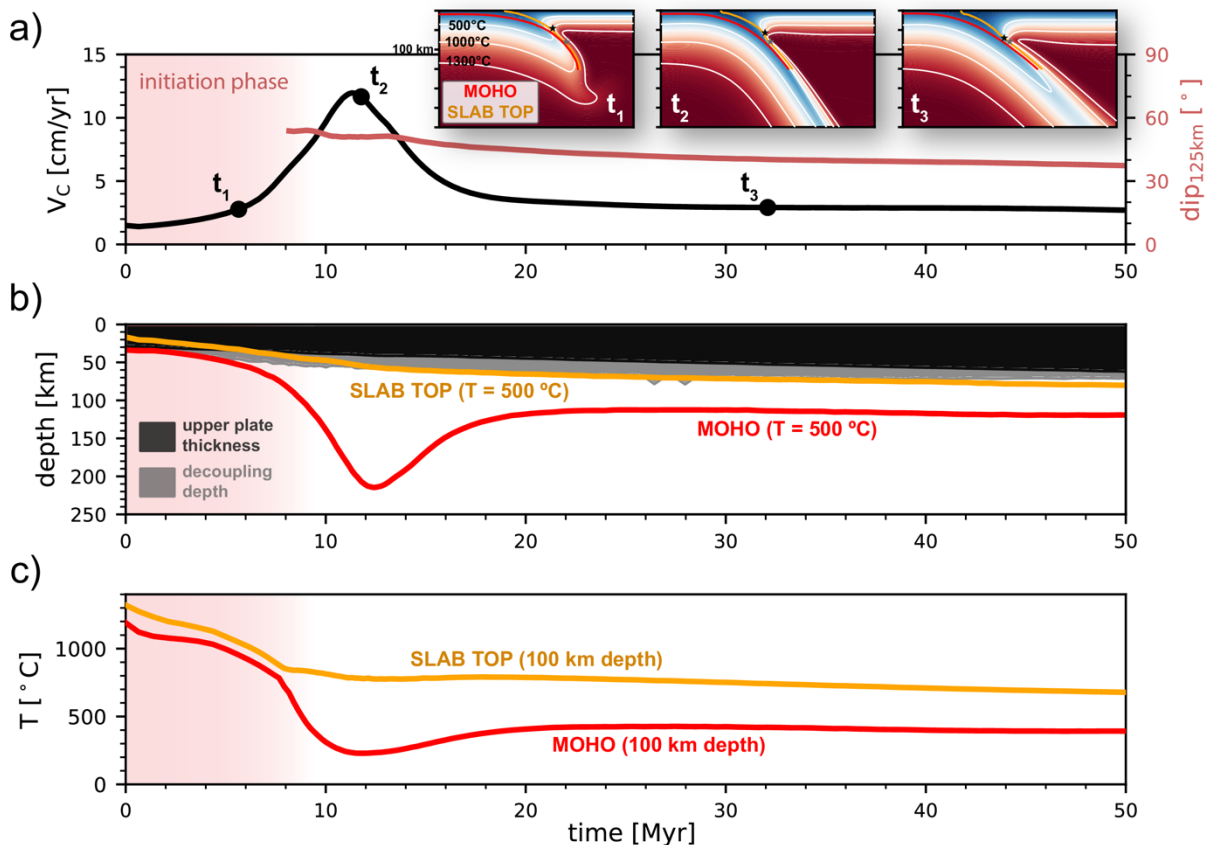


**Figure 2:** Temporal evolution of subduction properties. A) subduction zone convergence rate and shallow slab dip (at depth = 125 km), B) the depth of the 500 °C isotherm along the slab top and slab Moho and upper plate thickness and decoupling depth, C) the temperature at a depth of 100 km. Also, in A): Zoomed in snapshots of thermal structure for the three times shown in Figure 1 ( $t_1$ ,  $t_2$ ,  $t_3$ ) with slab Moho and slab top locations, the decoupling depth (black star), and maximum depth of decoupling (80 km, grey star).

339 The final “mature phase” begins as the slab impinges on the lower mantle at a depth of 660 km.  
 340 The viscous resistance of the strong lower mantle slows subduction to convergence rates of  $\approx 3$   
 341 cm/yr ( $v_{SP} \approx 1$  cm/yr,  $v_T \approx 2$  cm/yr) (Fig. 2a). Simultaneously, the slab leans back as  $v_T$   
 342 exceeds  $v_{SP}$  and slab evolution reaches a near-steady state with near-constant convergence rates.  
 343 The dislocation creep observed in the previous phase is now much more localized due to reduced  
 344 asthenospheric strain rates. Our third snapshot is at a model time of 32.1 Myr within this phase.  
 345 During the very lattermost stages of the model ( $> 65$  Myr), this near-steady state configuration is  
 346 disrupted when the strong, sub-crustal portion of the slab comes into contact with the overlying  
 347 fore-arc. This causes the convergence rate to further drop to  $\sim 1.5$  cm/yr.

348

### 349 **3.2. Thermal evolution**

350

351 We focus our analysis of the thermal evolution of the reference model on the temperatures at the  
 352 base (slab Moho) and upper surface (slab top) of the crust. At a given pressure, these two  
 353 temperatures bracket those that exhumed crustal rocks would be expected to experience. During  
 354 the subduction initiation phase, low convergence rates are accompanied by high slab Moho and  
 355 slab top temperatures. During the initiation snapshot ( $t = 5.6$  Myr), temperatures of 500 °C reach  
 356 depths as shallow as  $\approx 52$  km (1.7 GPa) along the slab Moho and  $\approx 33$  km (1 GPa) along the  
 357 slab top (Fig. 2b). Such warm temperatures are broadly consistent with petrologic observations  
 358 of warm conditions during the early stages of subduction (e.g., Platt, 1975; Cloos, 1985; Agard et  
 359 al., 2018).

360

361 Rapid cooling of both the slab Moho and slab top occur during the initiation phase, over  $\sim 8$   
 362 Myr, after which more protracted cooling persists for the rest of the model evolution.  
 363 Considering the slab top at a depth of 100 km, cooling of  $\approx 55$  °C/Myr occurs for the first 8 Myr.  
 364 After which, cooling is at the much lower rate of  $\approx 4$  °C/Myr (Fig. 2c). This can also be seen by  
 365 the gradual increase in depth of slab top isotherms throughout the 50 Myr of slab evolution (Fig  
 366 2b). From an initial depth of  $\approx 17$  km, the 500 °C isotherm reaches a depth of  $\approx 72$  km by the  
 367 time of our mature subduction snapshot (32.1 Myr).

368

369 This slab top temperature decrease can be linked to evolution of the thermal structure directly  
 370 overlying the slab which is, in turn, related to the upper plate thickness ( $h_{OP}$ ) and decoupling  
 371 depth (DD). As described the Section 2.4, the slab and wedge are decoupled at shallow depths  
 372 which causes a cold wedge corner to develop above the slab at depths  $< DD$ . In our models, we  
 373 do not specify the DD but track an equivalent depth that emerges self-consistently. Our DD is  
 374 taken to be where the mantle overlying our crust transitions down-dip from cold and strong ( $\eta >$

375  $2.5 \times 10^{22}$  Pa s) to hot and weak material ( $\eta \leq 2.5 \times 10^{22}$  Pa s). The DD increases through  
376 time, in part due to a gradual increase in  $h_{OP}$  (due to thermal thickening), until it approaches the  
377 imposed maximum depth of decoupling (MDD = 80 km) during the mature subduction phase  
378 (Fig. 2b). From then, it becomes approximately constant at  $\sim 75$  km (until the very end of the  
379 model,  $t > \sim 65$  Myr, when slab-forearc collision occurs). Cooling of the shallow portion of the  
380 slab top (i.e., slab top adjacent to the cold wedge corner) is caused by the thickening of this cold  
381 forearc region, which occurs with increasing DD and  $h_{OP}$ . The DD and  $h_{OP}$  control on slab top  
382 cooling is illustrated by the correspondence of the  $500^\circ\text{C}$  slab top isotherm depth with the DD  
383 (Fig. 2b), and that of the shallower,  $200^\circ\text{C}$  slab top isotherm with  $h_{OP}$  (Fig. S7).

384  
385 Inspecting pressure-temperature ( $P$ - $T$ ) profiles extracted from the slab top (Fig. 3a), cooling is  
386 demonstrated by the transition between hot  $P$ - $T$  profiles during the initiation phase, intermediate  
387  $P$ - $T$  profiles during free-sinking, and cold  $P$ - $T$  profiles during the mature phase. This causes the  
388  $P$ - $T$  profiles to sweep through much of the  $P$ - $T$  space associated with Agard et al.'s (2018)  
389 oceanic subduction exhumed rock compilation. All  $P$ - $T$  profiles exhibit increasing temperature  
390 with depth, with higher thermal gradients at shallower depths that transition into lower thermal  
391 gradients in the deeper mantle wedge. During the intermediate free sinking phase, for example,  
392  $dT/dz$  is  $\sim 12$   $^\circ\text{C}/\text{km}$  at depths less than 70 km. Deeper,  $dT/dz$  transitions to less than 5  $^\circ\text{C}/\text{km}$ .  
393 This kink occurs at a depth similar to the DD and becomes very pronounced as the DD  
394 approaches the MDD during mature subduction (Fig. 3a). This kinked  $P$ - $T$  profile shape is  
395 consistent with that observed in many kinematically-driven thermal models with imposed DD  
396 (e.g., Syracuse et al., 2010; van Keken et al., 2011). We also calculate the depth that initially flat-  
397 lying crust would reach during each model time-step and dash our  $P$ - $T$  profiles at depths beyond  
398 this (Fig. 3). For the conditions of interest ( $P < 4.5$  GPa), this is only important during the  
399 earliest stages of subduction, where the portion of the crust that was initially flat lying is  
400 shallower than the deepest compositional material that defines the weak interface. This is  
401 because this material is also used to define the deeper lithospheric shear zone that facilitates  
402 subduction initiation (Fig. 1a).

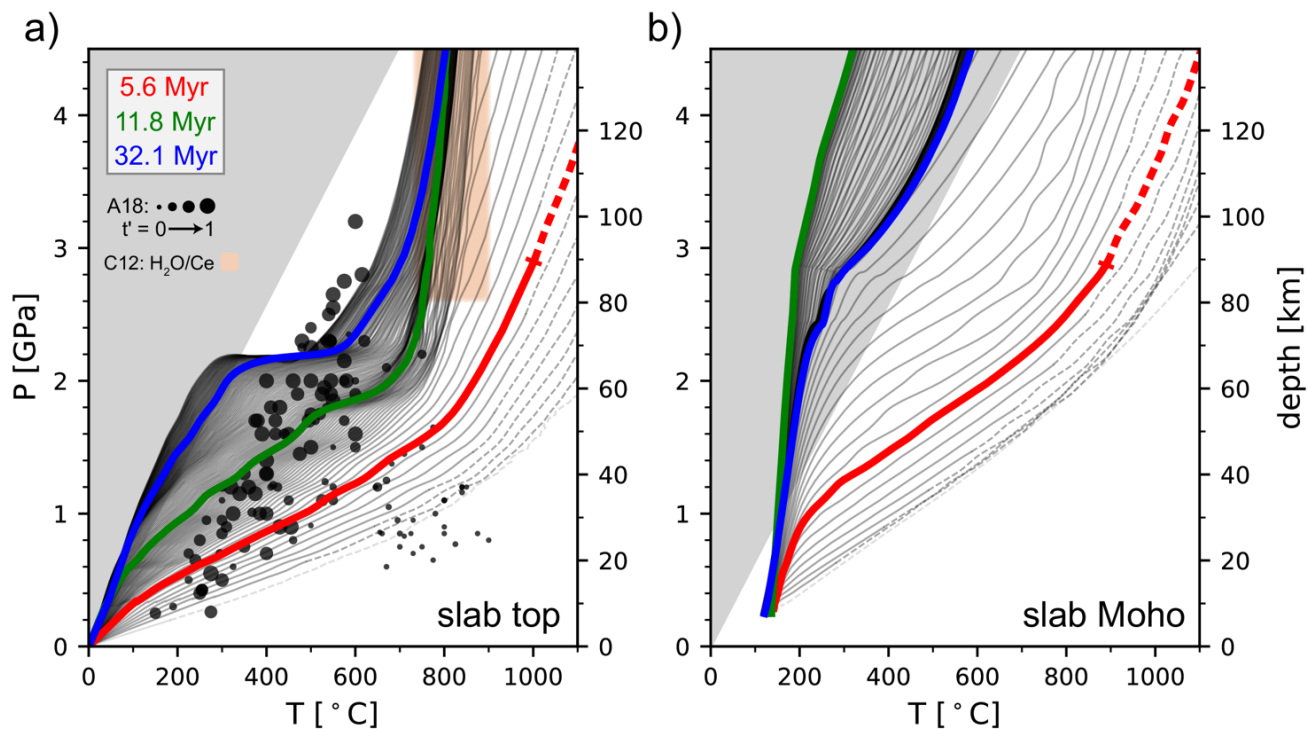


**Figure 3:** Temporal evolution of  $P$ - $T$  conditions along the model A) slab top, and B) slab Moho, with the three representative times highlighted (cf. Fig. 1). In addition to lithostatic pressure, dynamic pressure due to viscous flow is included in the extracted pressure. Agard et al’s (2018) compilation of the  $P$ - $T$  conditions recorded by rocks exhumed at oceanic subduction zones (point size represents the sample time relative to the lifetime of the corresponding subduction zone) and Cooper et al’s (2012) global range of sub-arc slab top temperatures (estimated using the  $H_2O/Ce$  thermometer on melt inclusions) is included in A. The gray region corresponds to average  $dT/dz < 5$  °C/km, i.e., the forbidden zone not represented in the exhumed rock record. These  $P$ - $T$  profiles have been smoothed using a Savitzky-Golay filter (see Fig. S4 for equivalent raw profiles). The first, faint profile corresponds to  $t = 0$  (i.e., the initial conditions), the total model time plotted is 52 Myr, and we dash profiles at depths greater than that which an initially flat-lying crust would reach.

403 The slab Moho temperature exhibits a more complex evolution. After rapid cooling during  
 404 subduction initiation, the Moho experiences additional cooling whilst the slab sinks rapidly  
 405 through the upper mantle during the free-sinking phase (Fig. 2). This free-sinking thermal  
 406 transient spans 5 to 10 Myr and is more pronounced at greater depth (i.e., for higher slab Moho  
 407 temperatures: Fig. S7). Slab Moho temperatures of 500°C, for example, are dragged down to  
 408 depths of 215 km during this phase, which is  $\sim 100$  km greater than the background cooling trend  
 409 (Fig. 2b). This cooling phase ends as the slab hits the upper-to-lower mantle viscosity jump and  
 410 the slab Moho temperatures increase in response to a rapid decrease in convergence rate.  $P$ - $T$   
 411 profiles extracted along the slab Moho show this transient as rapid steepening of  $P$ - $T$  profiles to  
 412 cold conditions during the free sinking phase (green profile; Fig. 3b) before rebounding to  
 413 warmer conditions (blue profile; Fig. 3b). For much of the model evolution, we note that slab  
 414 Moho  $P$ - $T$  profiles reside within the “forbidden zone” ( $dT/dz < 5$  °C/km) that is not represented  
 415 within the exhumed rock record. This is due to a combination of our old subducting plate age and

416 relatively high crustal thickness (initially 10 km but, in places, increasing to  $\approx$  15 km due to  
417 crustal thickening within the down-going slab).

418

### 419 **3.3. Dehydration evolution**

420

421 Coupling interpolated slab top and slab Moho  $P$ - $T$  paths with thermodynamic models of MORB  
422 and DMM reveal differences in dehydration evolution over the lifetime of a subduction zone  
423 (Fig. 4). This is due to a combination of the different  $P$ - $T$  paths a package of rock takes along the  
424 slab top versus the slab Moho (Fig. 3) and the stability of hydrous minerals within MORB and  
425 DMM across time varying  $P$ - $T$  conditions (Fig. S6). At the slab top, fluid saturated MORB  
426 dehydrates at shallower depths than DMM along the slab Moho for any given time step, and the  
427 two lithologies and thermal paths yield different locations and magnitudes of dehydration at  
428 various stages of subduction.

429

430 At the slab top, during the initiation phase of subduction, MORB releases  $H_2O$  in several large  
431 pulses ( $\sim$  1 - 2 wt%) at shallow forarc depths ( $>$  40 km) due to the relatively high geothermal  
432 gradient (Fig. 4a). As the subduction zone speeds up and cools during the free-sinking phase,  
433 dehydration depths increase, and multiple discrete dehydration pulses are transformed into a  
434 single large  $\sim$ 3.5-4.5 wt% release of  $H_2O$  corresponding to the blueschist to eclogite transition at  
435 depths of  $\sim$ 60 to 75 km (Fig. 4a; S6a). As the subduction zone reaches its mature phase, and the  
436 slab begins to interact with the lower mantle, dehydration from MORB at the slab top occurs at  
437 depths of 75 to 95 km releasing  $\sim$ 5 wt%  $H_2O$  over a narrow depth range into the subarc mantle  
438 (Fig. 4a).

439

440 Along the slab Moho, during the initiation phase (red line in Fig. 4b),  $H_2O$  saturated DMM  
441 releases  $H_2O$  in a gradual pulse of  $\sim$ 1.0 wt% at shallow depths from 50 to 60 km. This is  
442 followed by major dehydration of 7.5 wt%  $H_2O$  at depths of 75 - 80 km. The largest dehydration  
443 reaction represents the breakdown of serpentine and transformation of this phase into olivine  
444 (Fig. S6b). The depths of each pulse of dehydration become progressively deeper with increasing  
445 subduction age until at  $\sim$ 10 Myr when DMM remains hydrated past the range of our  
446 thermodynamic models and brings  $\sim$ 10 wt%  $H_2O$  deeper than 4.5 GPa ( $>$  150 km). This implies  
447 that, if the mantle is fully hydrated fully in some places, for example along bending faults formed  
448 near the trench (e.g., Grevenmeyer et al., 2018), vast quantities of water are transported past the  
449 subarc into the deeper portions of the mantle during intermediate and mature phases of  
450 subduction.

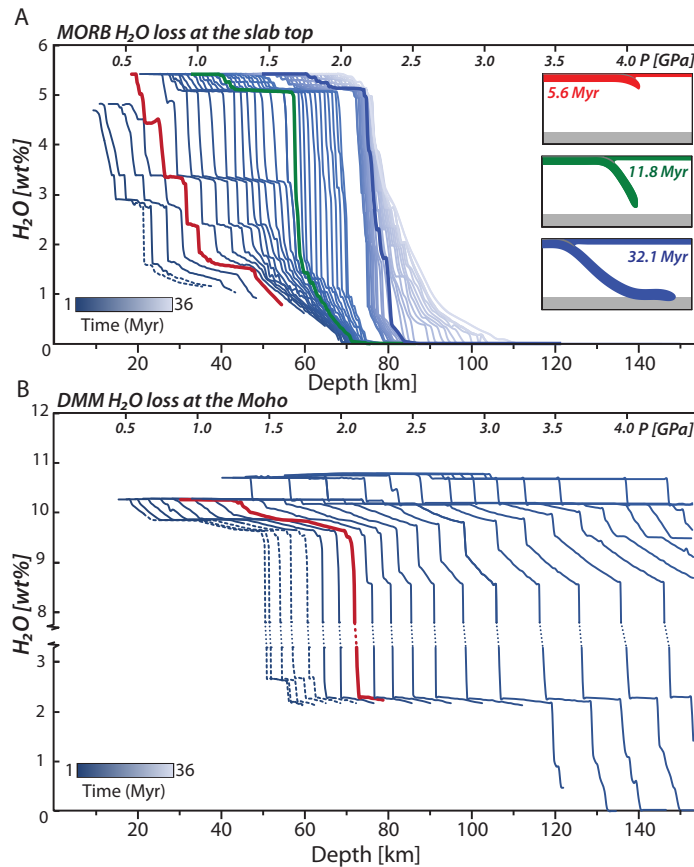


**Figure 4:** Dehydration during subduction shown as mineral bound H<sub>2</sub>O (wt%) versus depth and pressure. Dashed lines represent portions of the slab top and slab Moho that are not horizontal when the model starts. A) MORB mineral bound water evolution along the evolving slab top. Each line represents slab top MORB H<sub>2</sub>O loss at time slices of ~1 Myr intervals (every 100 model timesteps) starting at the left at 0.6 Myr. The bold colored lines represent mineral bound H<sub>2</sub>O at each of the three subduction stages in the inset corresponding to each color. B) DMM mineral bound H<sub>2</sub>O across the evolving slab Moho. Each line represents mantle lithosphere water loss at times slices of ~0.5 Myr intervals (every 50 timesteps) starting at the left at 0.6 Myr. Note after ≈ 10 Myrs DMM H<sub>2</sub>O loss at the slab Moho is no longer resolved in the thermodynamic P-T model space.

451 This has been suggested by previous workers (e.g., Hacker et al., 2008; van Keken et al., 2011;  
 452 Rüpke et al., 2004, Abers et al., 2017). Our analysis complements this previous work by  
 453 demonstrating that variable dehydration patterns are associated with a thermal structure that  
 454 evolves in a dynamically consistent fashion. It is also important to note that while we extract  
 455 mineral bound H<sub>2</sub>O along the slab top (Fig. 4a) and slab Moho P-T paths (Fig. 4b), the core of  
 456 the slab crust will have a thermal structure that is in between these two paths, while the core of  
 457 the subducting oceanic lithosphere will be colder than the slab Moho. Thus, dehydration from  
 458 slab crust core and mantle core will occur at slightly different depths, ultimately resulting in a  
 459 smearing out of dehydration loci between these two end members.

### 460 3.4. Variable subduction parameters

461  
 462 To explore whether the reference model behavior is representative of a broader subduction zone  
 463 parameter space and develop further intuition about links between time-dependent thermal  
 464 structure and slab evolution, we have examined the effects of additional subduction properties.  
 465 Figure 5 show the thermal evolution as a function of three subduction properties that are  
 466 relatively uncertain or may vary substantially in nature: slab, crust, and lower mantle viscosity.  
 467 To investigate these properties, we focus on the slab Moho and slab top temperatures at  
 468 relatively shallow depths (60 km and 100 km) and examine how the dependence of such



469 temperatures on physical subduction parameters vary relative to the reference (black profile in  
 470 each panel of Figure 5).

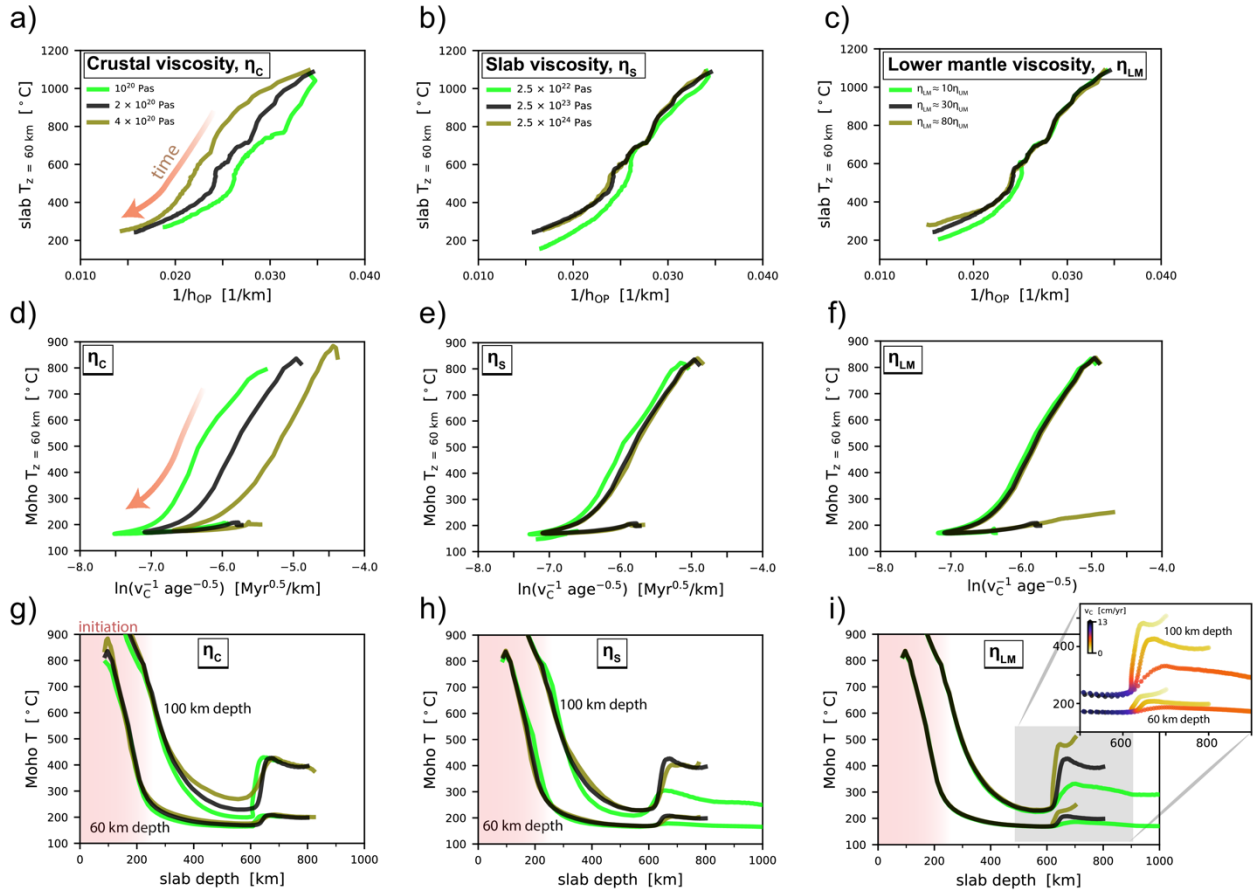


**Figure 5:** Subduction zone temperature as a function of kinematic subduction properties for variable model parameters. Models have variable crust viscosity, slab viscosity, and lower mantle viscosities, with the reference model plotted in black. A-C) Slab top temperature (depth = 60 km) as a function of the reciprocal of upper plate thickness, D-F) slab Moho temperature (depth = 60 km) as function of  $\log(v_c^{-1} \text{age}^{-0.5})$  (Mauder et al., 2019), and G-I) slab Moho temperature (depths = 60 km, 100 km) as a function of slab depth. Panel I) includes a zoom in corresponding to the time of slab interaction with the viscous lower mantle (points colored by convergence rate). Note that time-dependent dislocation creep produces a time-dependent upper-to-lower mantle viscosity ratio; the quoted values (10, 30, 80) are averaged over the mature phase of subduction.

471 As in the reference case, slab top temperature exhibits a strong dependence on the overriding  
 472 plate thickness ( $h_{OP}$ ), and interrelated DD, within all models. To first order, the inverse  
 473 relationship between slab top temperature and  $h_{OP}$  is approximately linear (Fig. 5a-c). On top of  
 474 this relationship is, in some cases, a shift related to convergence rate ( $v_c$ ). High convergence  
 475 rates transport cold surface temperatures down to the depth of interest more rapidly, thereby  
 476 producing colder slab top temperatures for a given  $h_{OP}$ . Models with either weak crusts (Fig. 5a)  
 477 or weak slabs (Figs. 5b, S8) exhibit faster convergence rate and hence cooler slab tops. A weaker  
 478 lower mantle produces more rapid convergence, and cooler slab tops, only during the mature  
 479 subduction phase (Figs. 5c, S9).

480

481 In all models, slab Moho temperature exhibits a negative correlation with the “thermal  
 482 parameter” (Kirby, 1996) that combines plate age ( $t$ ), convergence rate ( $v_C$ ), and dip (cf., van  
 483 Keken et al., 2011). In our analysis, we adopt the modified form of Maunder et al. (2019),  $\phi =$   
 484  $v_C^{-1}t^{-0.5}$ , which is applicable to regions where slab temperatures are dominantly velocity  
 485 controlled and produces a positive temperature correlation. Figure 5d-f shows how slab Moho  
 486 temperature varies as a function of the logarithm of this thermal parameter. During the first two  
 487 subduction phases, slab Moho temperature decreases rapidly as  $\ln(\phi)$  decreases ( $v_C$  increases) in  
 488 all models (Fig. 5d-f). As the slabs hit the lower mantle, the strength of the dependence of Moho  
 489 temperature on  $\ln(\phi)$  reduces:  $\phi$  increases rapidly as the slab hits the lower mantle ( $v_C$   
 490 decreases), but the Moho temperature does not increase to the extent expected from the main  
 491 trend. This is due to the thermal thickening of the upper plate and associated increase in the  
 492 decoupling depth (DD). As the DD approaches, and then exceeds, the 60 km depth of interest,  
 493 the rate of thermal diffusion into/out of the slab Moho region, and hence the slab Moho  
 494 temperature, decreases. The subsequent reduction in slab Moho temperature dependence on  $v_C$  is  
 495 in line with Maunder et al.’s (2019) suggestion that crustal temperatures at depths  $<$  DD are  
 496 largely independent of  $v_C$  (i.e., the temperature is slab age controlled). This illustrates the  
 497 importance of non-steady state thermal structure inherited from previous subduction phases. For  
 498 models with varying  $v_C$ , a shift to higher Moho temperatures occurs for higher  $v_C$  (e.g., Fig. 5d).  
 499 This stems from the model initial conditions, where temperature is prescribed (i.e., constant) but  
 500  $\phi$  is calculated dynamically (i.e., variable  $v_C$  produces variable  $\phi$ ).

501

502 All slab Moho temperatures reduce during the free-sinking phase and then increase following the  
 503  $v_C$  reduction as the slab hits the strong lower mantle (Fig. 5g-i). Slab Moho temperatures during  
 504 the free-sinking phase are lowest for the fastest subduction zones (e.g., weak slab or weak crust)  
 505 and, upon slab interaction with the lower mantle, the temperature increase is greatest for  
 506 subduction zones with the largest  $v_C$  reduction (e.g., models with a strong lower mantle: Fig. 5i).

507

### 508 **3.5. Variable decoupling parameterization**

509

510 We now examine the effect of variable crustal decoupling parameterizations on slab thermal  
 511 structure. These tests are motivated by considerable uncertainty regarding the physical  
 512 mechanism responsible for the decoupling-to-coupling transition. In addition to cutting off the  
 513 isoviscous crust at 80 km (i.e., our reference model), we examine cases where the crust is cutoff  
 514 at a greater depth (200 km) and where the crust has a visco-plastic rheology. As detailed in  
 515 Section 2.4, the low plastic yield stress of the visco-plastic crust is one mechanism to self-  
 516 consistently mimic a transition from shallow decoupling to deep coupling in numerical models  
 517 (Figs. 6c, S10, Maunder et al., 2018). The three parameterizations produce similar slab top  $P$ - $T$   
 518 profiles during the initiation and free sinking phases (Fig. 6). This follows from the nearly  
 519 equivalent DDs that emerge during these earlier phases (e.g.,  $\approx$  60 km during free sinking). The  
 520 precise timing of the various phases is the only minor source of variability. In the visco-plastic

521 crust case, subduction initiation is about 2 Myr slower which causes these thermal phases to  
 522 occur 2 Myr later than in the isoviscous crust cases (Fig. S11).

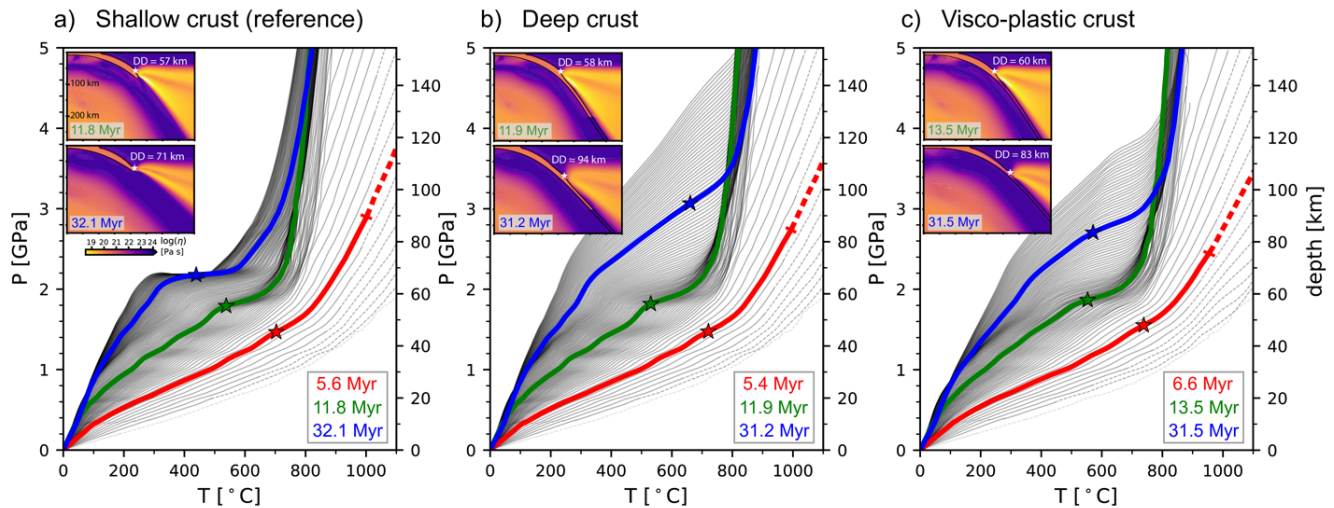


**Figure 6:** Comparison of slab top pressure-temperature evolution for variable crustal parameterizations: A) Isoviscous crust cut-off at 80 km depth (reference model), B) isoviscous crust cut-off at 200 km depth, C) visco-plastic crust. Insets show viscosity structure zoomed into the trench region during free sinking (green) and mature phases (blue). Overlain are the decoupling depths calculated as described in Section 3.2. For all models,  $P$ - $T$  profiles are plotted for between 52 and 54 Myrs of subduction evolution.

523 More significant variability occurs during the mature phase of subduction, during which the DD  
 524 varies significantly between parameterizations. After  $\approx 40$  Myr of evolution and upper plate  
 525 thickening, the DD in the shallow crust cutoff case reaches a near constant  $\approx 75$  km (as the DD  
 526 approaches the imposed maximum depth of decoupling of 80 km). In contrast, in the other two  
 527 cases, the DD continues to increase during the mature phase. This increase in DD corresponds to  
 528 thickening of the cold mantle wedge corner which produces continuously cooling slab tops in  
 529 these two models (Fig. 6b,c). DD increase is most rapid in the deep crust cutoff model, relative  
 530 to the visco-plastic case, which is reflected in more rapid slab top cooling (Fig. S11). This  
 531 contrasts with the thermal conditions reached during the mature phase of the reference case  
 532 which exhibit only very minor slab top cooling (Fig. 6a). The evolution of slab Moho  $P$ - $T$   
 533 conditions follows a comparable trend. While all  $P$ - $T$  profiles are comparable before  $\sim 30$  Ma,  
 534 the two additional tests exhibit significant slab Moho cooling after this time while the shallow  
 535 crust cutoff case does not (Fig. S12).

536

## 537 4. DISCUSSION

538

### 539 4.1. Dynamically evolving thermal structure

540

541 Previous studies have mapped out the dependence of subduction zone thermal structure on  
 542 subduction parameters using models of mantle wedge flow driven by imposed subduction

543 velocity, slab dip, and overriding plate thermal structure (e.g., Wada and Wang, 2009; Syracuse  
544 et al., 2010). Time-dependent thermal structure can be introduced within this type of  
545 kinematically-driven modeling approach by imposing time-varying slab properties and/or  
546 inspecting thermal evolution prior to steady-state (e.g., Peacock and Wang, 1999; Hall, 2002;  
547 van Keken et al., 2018; Suenaga et al., 2019). However, such approaches are unable to ensure  
548 that the slab, plates, and mantle wedge co-evolve in a dynamically consistent manner, and in the  
549 case of steady-state models, resolve transient thermal effects. Motivated by this, we have used  
550 dynamically consistent subduction models to probe the co-evolution of subduction zone  
551 properties and slab thermal structure. Our modeling approach has similarities to that of Arcay  
552 (2012; 2017) and Kincaid and Sacks (1997), in that we investigate time-dependent thermal  
553 structure in models that solve for thermo-mechanical deformation in a region extending beyond  
554 the mantle wedge and, as in Kincaid and Sacks (1997), we do not impose plate velocities.  
555 Kincaid and Sacks (1997) demonstrate that significant slab top temperature variability can occur  
556 through time in their numerical models. Driven by dynamic variability in subduction parameters  
557 like convergence rate (e.g., Clark et al., 2008; Cerpa et al., 2014), we also observe a strong time  
558 dependence of modeled slab pressure-temperature ( $P$ - $T$ ) conditions. By expanding these  
559 modeling studies to a large model domain, with self-consistently evolving trenches and crustal  
560 geometries, we are able to further elucidate the links between mantle-scale subduction evolution  
561 and subduction zone thermal structure.

562  
563 The links between slab temperature and subduction kinematics in our models are in general  
564 agreement with previous studies. The primary control on slab Moho temperature is convergence  
565 rate, as has been demonstrated extensively within kinematically-driven thermal models (e.g.,  
566 Peacock, 1991; Peacock and Wang, 1999; Van Keken et al., 2002). When coupled with a  
567 dynamically evolving slab, this results in a pulse of the coldest slab Moho temperatures during  
568 the “free-sinking” phase of subduction: i.e., the fastest subduction phase before the slab impinges  
569 on the lower mantle. In addition to the time dependence of subduction parameters, non-steady  
570 thermal structure from previous subduction phases impacts slab temperatures at any given time.  
571 For example, as the slab hits the lower mantle, the convergence rate decreases to the few cms/yr  
572 rate observed during the subduction initiation phase. As expected, the slab Moho temperature  
573 increases as the convergence rate decreases. However, this occurs by  $\sim 100$  °C less than expected  
574 following a basic scaling with a modified thermal parameter (Fig. 5d-f). This is likely due to the  
575 gradual development of a larger cold wedge corner, as the upper plate ages and thickens, which  
576 overlies the slab at shallow depths and reduces slab Moho (and slab top) temperatures. This  
577 illustrates the importance of the non-steady state component of subduction zone thermal  
578 structure.

579  
580  $P$ - $T$  conditions along the slab top are primarily controlled by the depth extent of the cold wedge  
581 corner region overlying the slab. As the overriding plate ages, its thickness and the DD increases,  
582 both of which increase the size of the cold wedge corner and produce slab top cooling. While  
583 such a dependence of slab top  $P$ - $T$  on the decoupling depth (DD) has been shown in

584 kinematically-driven models (Syracuse et al., 2010; Maunder et al., 2019; Perrin et al., 2018), an  
585 important distinction is that our DD evolves in a dynamically consistent manner. The DD, which  
586 marks the down-dip transition from cold/strong to hot/weak wedge material, exhibits significant  
587 variation throughout the model evolution (Fig 6a). While this appears at odds with previous  
588 suggestions of a near-uniform DD (~ 80 km), based on surface heat flow measurements and first-  
589 order petrological constraints (Tatsumi, 1986; Furukawa, 1993; Wada and Wang, 2009), we note  
590 that any global survey of present-day subduction zones is naturally skewed away from the initial  
591 subduction phases that exhibit the most DD (and slab top temperature) variability. Our models  
592 predict that the high temperatures recorded within early stage exhumed rocks (e.g., Platt, 1975;  
593 Cloos, 1985; Agard et al., 2018; 2020) coincide with the very low DDs that occur before the cold  
594 nose of the mantle wedge has had time to thicken substantially (i.e., during the initiation phase).  
595 This early-stage cooling (at a given depth) is in agreement with previous dynamic (Kincaid and  
596 Sacks, 1997; Yamato et al., 2007) and kinematic-dynamic (e.g., Hall, 2012; van Keken et al.,  
597 2018) modeling studies.

598

599 In the mature stage of our reference model, the DD and slab top  $P$ - $T$  conditions exhibit minimal  
600 variability (Figs. 3, 6a). This is because the DD is capped at the depth that we cut off our weak  
601 crust (i.e., maximum depth of decoupling, MDD = 80 km). In models that do not impose such a  
602 MDD (Fig. 6b, c), the DD continues to increase during the model run (cf. Kincaid and Sacks,  
603 1997). The average depth to slab top beneath active volcanic arcs is on the order of 100 km  
604 (England and Katz, 2010), which presents an issue for the later stages of such models where the  
605 DD increases to substantially greater than 100 km (as mantle wedge partial melting requires a  
606 hot, sub-arc source region). We therefore focused on our model with a shallow crust cutoff, with  
607 an 80 km cutoff depth comparable to that of previous studies (e.g., Wada and Wang, 2009;  
608 Syracuse et al., 2010), but note that our decoupling parameterization only impacts thermal  
609 evolution during very mature subduction. In nature, this ~ 80 km MDD is likely dictated by a  
610 switch from rheologically weak hydrous phases to rheologically strong anhydrous phases in  
611 either the crust (i.e., as parameterized in our models) or in the mantle wedge (e.g., Hacker et al.,  
612 2003; van Keken et al., 2011; Hirauchi and Katayama, 2013; Agard, 2020; Peacock and Wang,  
613 2020). Given the strong temperature dependence of dehydration reactions (Fig. S6), and  
614 continually evolving thermal conditions (e.g., Fig. 3), this depth can be expected to vary  
615 substantially through a subduction zone's lifetime (e.g., Agard et al., 2020)

616

## 617 **4.2. Comparison of modeled and Earth subduction zones**

618

619 To check that our reference model is aligned with subduction observables, we compare the  $P$ - $T$   
620 conditions of our model with global compilations of those suggested by exhumed rocks and by  
621 melt inclusions within arc eruptives (Fig. 3). Our slab top temperatures are within the global  
622 range of sub-arc slab top temperatures estimated by applying the  $H_2O/Ce$  thermometer to melt  
623 inclusions (Cooper et al., 2012: 733 – 901 °C at depths of 80 – 169 km) and, as discussed in  
624 more detail in Section 4.4.1, our slab Moho and slab top profiles sweep through much of the  $P$ - $T$

625 space represented by metamorphic rocks exhumed at oceanic subduction zones (Agard et al.,  
626 2018).

627  
628 Due to the generic nature of our models, it is inappropriate to use this model as a direct proxy for  
629 any specific Earth subduction zone. However, to again check the first-order behavior, we  
630 conduct a cursory comparison with subduction in Northeast Japan (Honshu). Japan is chosen as  
631 it contains a similarly old subducting plate (130 Ma relative to 121 Ma), a young upper plate, and  
632 a similar mode of subduction (slab flattened above the lower mantle) as produced in the mature  
633 phase of our model. Relative to this mature phase, the main differences are lower modeled  
634 convergence rates ( $\approx 3$  cm/yr) than observed ( $\approx 8$  cm/yr) and a younger modeled subduction  
635 duration (32 Myr) than that suggested by Jurassic volcanic deposits (Miyazaki et al., 2016).  
636 Regarding the latter, we note that Izanagi-Pacific ridge subduction is likely to have partially reset  
637 the thermal structure at  $\sim 50$  Ma (Wu and Wu, 2019) so that the effective thermal age is closer to  
638 that of our models. Earlier in the model evolution, towards the end of the free-sinking phase, we  
639 have equivalent convergence rates ( $\approx 8$  cm/yr at  $t \approx 14$  Myr) but a slab morphology less similar  
640 to that of the Japan slab (i.e., without a flat slab).

641  
642 During the mature phase, modeled surface heat flow is comparable with that of Northeastern  
643 Japan. Excluding local variability due to shallow magmatic intrusion, the surface heat flow  
644 increases by about  $50$  mW/m<sup>2</sup> from forearc to arc (Tanaka et al., 2004; Wada and Wang, 2009).  
645 Our models exhibit a similar,  $\approx 55$  mW/m<sup>2</sup> forearc-to-arc increase in surface heat flow.  
646 Considering arc location, the depth to slab top beneath the Japan volcanic arc is  $\approx 95$  km  
647 (England and Katz, 2010). If we assume a simple parameterization of thermally controlled  
648 mantle wedge melting, which focuses partial melting at the trench-ward extent of temperatures  
649 between  $1200$  °C and  $1350$  °C (e.g., Tatsumi, 1986; Kelemen et al., 2003), we can estimate an  
650 equivalent model depth. For the mature phase, the trench-ward extent of the  $1200$  °C isotherm  
651 corresponds to a depth to slab top of  $88$  km and, for the  $1300$  °C isotherm, this depth is  $101$  km  
652 (Fig. S13). Both are comparable to the  $\approx 95$  km observed. During the end of the free-sinking  
653 phase, where convergence rate is equivalent to that of Northeastern Japan ( $\approx 8$  cm/yr) but slab  
654 morphology and subduction duration are less similar, our modeled mantle wedge is hotter than  
655 that suggested by arc location and heat flow. This is demonstrated by a shallower sub-arc depth  
656 to slab top ( $\approx 80$  km using the  $1300$  °C isotherm) and elevated forearc-to-arc surface heat flow  
657 increase ( $\approx 85$  mW/m<sup>2</sup>). It therefore appears that, during this earlier phase, the close proximity to  
658 (hot) subduction initiation is the main factor behind this discrepancy. During the more mature  
659 phase, the more comparable slab age and subduction duration produce a better thermal fit despite  
660 the lower model convergence rate.

661  
662 These comparisons illustrate the challenges associated with attaching dynamic and time-  
663 dependent models to specific subduction zones. Despite this, the first-order agreement gives us  
664 confidence in the general applicability of our models to understanding the time-dependent  
665 thermal evolution of Earth subduction zones.

666

### 667 **4.3. Limitations of our approach**

668

669 To target first order relations, we neglect a number of processes that impact subduction zone  
670 thermal structure. Here, we point out a selection of these processes. Regarding heat transport,  
671 mantle flow in the 3<sup>rd</sup> dimension (e.g., Kincaid and Griffiths, 2003; Plunder et al., 2018) and melt  
672 and fluid flow (e.g., Rotman and Spinelli, 2013) have both been shown to exert a control in  
673 previous modeling studies. Small-scale convection (e.g., Honda and Saito, 2003; Davies et al.,  
674 2016) and buoyant upwellings of meta-sedimentary plumes or diapirs (Gerya and Yuen, 2003;  
675 Behn et al., 2011) may also play a role. Furthermore, radiogenic and shear heating and are two  
676 important heat sources that can be expected to increase subduction zone temperatures relative to  
677 those modeled here. Shear heating has been shown to elevate slab top temperatures particularly  
678 within the relatively shallow portion of the forearc that undergoes brittle/frictional deformation  
679 (e.g., Molnar and England, 1990; Peacock, 1992; Gao and Wang, 2014).

680

681 It is with these simplifications in mind that we have focused on relative temperature variation as  
682 a function of time, as opposed to absolute temperatures. We speculate that most of these  
683 complexities will increase the time dependence of subduction zone thermal structure, as a result  
684 of the additional dependencies of time evolving properties like convergence rate on such  
685 complexities. As we progress to applying dynamic models to the thermal structure of specific  
686 subduction zones, an assessment of the importance of such complexities within a particular  
687 setting will be critical.

688

### 689 **4.4. Geologic implications**

690

691 Temporal changes of subduction zone thermal structure can be expected to be imprinted on a  
692 large number of geological phenomena. Here, we briefly discuss two: time-dependent changes in  
693 the pressure-temperature conditions of exhumed metamorphic rocks, and in the metamorphic  
694 dehydration reactions experienced by the down-going oceanic lithosphere.

695

#### 696 *4.4.1. Comparison to the exhumed rock record*

697

698 In the case of exhumed metamorphic rocks, recorded temperatures are generally 100 - 300 °C  
699 warmer (Penniston-Dorland et al., 2015) than the equivalent depth temperatures generated with  
700 kinematically driven models of slab zone thermal structure (Gerya et al., 2002; Syracuse et al.,  
701 2010). The temperature discrepancy is reduced when continental rocks are omitted from  
702 compilations (Agard et al., 2018), but certain models remain colder than the rocks (Syracuse et  
703 al., 2010). Inspired by the possibility that metamorphic rocks could be preferentially exhumed  
704 during certain, anomalously hot, subduction phases (e.g., Abers et al., 2017; van Keken et al.,  
705 2018), we overlay Agard et al.'s (2018) exhumed rock compilation on our modeled slab top *P-T*  
706 evolution that consists of various dynamic subduction phases (Fig. 3a). Initially, modeled slab

707 top temperatures overlay the hottest metamorphic soles associated with the early stages of  
708 subduction (e.g., Platt, 1975; Cloos, 1985; Agard et al., 2018). Subsequently, slab top  
709 temperatures sweep through much of the  $P$ - $T$  space covered by colder rocks exhumed during  
710 sustained subduction. Because we consider a generic subduction zone, with simplifying  
711 assumptions, we cannot assess  $P$ - $T$  conditions related to specific regions and/or the contribution  
712 of additional heat sources (e.g., shear heating, radiogenic heating, fluid transport). However, this  
713 demonstrates that dynamic variability in slab evolution can produce a wide range of  $P$ - $T$   
714 conditions over the history of even a single subduction zone.

715

716 Moreover, the various thermal phases of our dynamic models may have an effect on the  
717 likelihood of rock recovery at various times during subduction. Agard et al. (2009; 2018) show  
718 that the exhumed rock record is dominated by early (initiation) and late stage (mature)  
719 exhumation and that intermediate stage rocks are underrepresented. In our models, the  
720 intermediate stage is associated with rapid convergence rates and anomalously cold slab Moho  
721 temperatures (Fig. 2). While we do not model any of the processes related to rock detachment  
722 and exhumation (e.g., Gerya et al., 2002; Yamato et al., 2007; Ruh et al., 2015), both low  
723 temperatures and rapid rates could indeed have a negative effect on rock detachment (Ruh et al.,  
724 2015; Agard et al., 2018). Taken together, and as recently discussed by Peacock (2020), our  
725 dynamic models emphasize the importance of identifying the specific phase of subduction during  
726 which rocks of interest were exhumed.

727

#### 728 *4.4.2. Dehydration of oceanic lithosphere*

729

730 Coupling these thermal structures to thermodynamic models of MORB and DMM yields patterns  
731 of metamorphic dehydration that are also time-dependent, due in large part to the strong control  
732 of temperature on devolatilization reactions. The location and magnitude of dehydration from  
733 oceanic lithosphere has important implications for a range of geodynamic, geochemical, and  
734 tectonic processes (e.g., Peacock, 2001; Hacker et al., 2003; Bebout, 2007). During the initiation  
735 phase of subduction, due to the warm slab top, all mineral-bound  $H_2O$  is lost from the  
736 downgoing oceanic crust at shallow forearc depths (Fig. 4a), delivering ample serpentizing  
737 fluid to the developing cold mantle wedge corner. Using a similar approach, Abers et al., (2017)  
738 surmised that cold mantle wedges would only be hydrated in the warmest subduction zones and  
739 presented geophysical data for serpentized mantle wedge in the warm Cascadia subduction  
740 zone. At the slab Moho during this initiation phase,  $H_2O$  is lost from any hydrated lithospheric  
741 mantle at subarc depths due to a combination of a colder slab Moho  $P$ - $T$  path than slab top, and  
742 the stability fields of hydrous phases in DMM (Figs. 3, 4b, S6). This implies that fluids in arc  
743 source regions are sourced from the devolatilization of ultramafic mantle during the initial stages  
744 of subduction (e.g., Rüpke et al., 2004).

745

746 In the intermediate and mature phases of subduction, our analysis indicates that MORB  
747 dehydration at the slab top releases up to 5 wt%  $H_2O$  between 80-90 km, providing the likely



748 source fluids for partial melting in the subarc mantle (Fig. 4a). At the same time, because the slab  
749 Moho has cooled considerably during the free sinking phase, hydrous minerals (antigorite)  
750 within our thermodynamic model space do not warm up enough to break down during the mature  
751 phase of subduction. Therefore, any hydrated mantle at the slab Moho and within the core of the  
752 mantle lithosphere of the slab will be carried past  $\sim 4.5$  GPa ( $> 150$  km) (e.g., Figs. 4b, S6) and  
753 delivered to the deeper mantle.

754  
755 Other workers have suggested this same trend of dehydration of MORB along the slab top at  
756 subarc depths within intermediate to cold subduction zones, while oceanic mantle lithosphere  
757 likely carries fluids beyond the arc into the mantle (e.g., Hacker et al., 2008; van Keken et al.,  
758 2011; Grove et al., 2012; Rüpke et al., 2004). Our results complement this previous work, which  
759 focused on kinematic-dynamic models, by providing a dynamic framework for the variability  
760 that these dehydration patterns may exhibit during subduction zone evolution. Of course, our  
761 analysis is limited by the assumption of fluid saturation, which while likely appropriate for the  
762 slab top based on geologic observations (e.g., Bebout and Penniston-Dorland, 2016), is not likely  
763 for the mantle lithosphere or the gabbroic core the subducting oceanic crust (e.g., Faccenda,  
764 2014). The degree and distribution of hydration within the subducting slab mantle is likely  
765 controlled by the degree and depth of fluid infiltration along fractures formed as the slab bends  
766 before the trench (e.g., Naif et al., 2015; Korenaga, 2017), or the subduction of hydrated oceanic  
767 transform zones (e.g., Prigent et al., 2020). This analysis also assumes chemical equilibrium, the  
768 limitations of which are discussed in Condit et al. (2020). Variation in sea floor alteration and  
769 metasomatism can influence the composition of subducting oceanic crust and manifest in subtle  
770 variations in dehydration locations and magnitudes (e.g., Hernandez-Urbe et al., 2020).  
771 However, even given these caveats, our analysis demonstrates that the time evolving thermal  
772 structure of dynamic subduction zones can be expected to manifest in strong temporal variation  
773 in crust and mantle dehydration during the lifetime of a subduction zone, and that this temporal  
774 variation in dehydration is broadly in agreement with geological observations.

## 775 776 **5. CONCLUSION**

777  
778 We have used time evolving and dynamically consistent numerical models to explore how  
779 subduction zone thermal structure evolves over the lifetime of a subduction zone. We find that  
780 pressure-temperature ( $P$ - $T$ ) conditions along the slab Moho and slab top exhibit substantial  
781 variability through during the phases of subduction: initiation, free sinking, and mature  
782 subduction. This variability occurs in response to temporal changes in subduction properties  
783 (e.g., fast convergence during free sinking vs. slow convergence during mature subduction), and  
784 the inheritance of thermal structure from previous subduction phases (e.g., due to forearc  
785 thickening).

786  
787 During subduction initiation, slab Moho and slab top temperatures both decrease rapidly at a  
788 given depth. After which, slab Moho temperatures exhibit an additional cooling phase associated

789 with rapid convergence rates during the slab's free sinking phase. Once the slab impinges on the  
790 strong lower mantle, convergence rate reduces, and significant cooling terminates. Slab top  
791 temperatures are less dependent on convergence rate but strongly dependent on the vertical  
792 extent of the cold and stiff mantle wedge corner. In our models, the vertical extent of this region  
793 increases as the upper plate progressively ages and thickens. This imparts a cooling trend on the  
794 slab top that, in the case of our reference model with a crust that is cutoff at 80 km depth, persists  
795 until the geometry of this wedge corner region reaches near steady state during mature  
796 subduction.

797  
798 This dynamic temperature evolution manifests in a range of geological observables. In addition  
799 to confirming first order model agreement with surface heat flow measurements, arc locations,  
800 and slab  $P$ - $T$  estimates from melt inclusion geochemistry, the  $P$ - $T$  conditions experienced by the  
801 slab top of our reference model sweep through much of the  $P$ - $T$  space recorded by exhumed  
802 rocks during  $\sim 50$  Myrs of modeled subduction evolution. In addition to substantiating previous  
803 suggestions that variability in the exhumed rock record could relate to various dynamic phases of  
804 subduction evolution, evolving  $P$ - $T$  conditions imply large variability in the location and  
805 magnitude of oceanic lithosphere dehydration over the lifetime of a subduction zone. In the early  
806 stages of subduction, hydrated mantle lithosphere at the slab Moho provides the bulk of hydrous  
807 fluids at subarc depths, while MORB at the slab top dehydrates at shallow forearc depths. During  
808 the free sinking and mature phases, MORB releases water at near to subarc depths, while  
809 hydrated ultramafic rocks along the slab Moho carry fluids into the deeper mantle well beyond  
810 the subarc region. This simple analysis indicates that time-dependent thermal structure has  
811 profound impacts on the global water cycle and fluids in arc source regions.

812  
813 This work emphasizes the need to consider subduction zone thermal structure as dynamically  
814 evolving. Parameterization of this dynamic evolution is required to extrapolate inferences about  
815 modern subduction behavior, like slab dehydration, into the geological past. To accurately  
816 interpret observables originating from earlier in a subduction zone's lifetime, consideration of  
817 the dynamic subduction phase associated with the origin of that particular observable is needed.

## ACKNOWLEDGEMENTS

This work has benefited from scientific discussions with Ben Klein, Victor Guevara, Mélanie G erault, Thorsten Becker, Whitney Behr, and Leigh Royden. We also thank Simon Peacock and an anonymous reviewer for constructive comments that significantly improved the manuscript. The computations of this work used the Extreme Science and Engineering Discovery Environment (XSEDE), which is supported by National Science Foundation (NSF) grant number ACI-15485x62. We also thank the Computational Infrastructure for Geodynamics ([geodynamics.org](http://geodynamics.org)), which is funded by the NSF under awards EAR-0949446 and EAR-1550901, for supporting the development of ASPECT. The ASPECT files needed to run the models are

available in the following permanent Zenodo repository  
(<https://doi.org/10.5281/zenodo.4543413>).

## REFEERENCES

- Abers, G.A., Van Keken, P.E., Hacker, B.R., 2017. The cold and relatively dry nature of mantle forearcs in subduction zones. *Nature Geoscience*, 10, 333–337.  
<https://doi.org/10.1038/ngeo292>
- Agard, P., Plunder, A., Angiboust, S., Bonnet, G., Ruh, J., 2018. The subduction plate interface: rock record and mechanical coupling (from long to short timescales). *Lithos*, 320–321, 537–566. <https://doi.org/10.1016/j.lithos.2018.09.029>
- Agard, P., Prigent, C., Soret, M., Dubacq, B., Guillot, S., Deldicque, D., 2020. Slabification: Mechanisms controlling subduction development and viscous coupling. *Earth-Science Reviews*, 208, <https://doi.org/10.1016/j.earscirev.2020.103259>
- Agard, P., Yamato, P., Jolivet, L., Burov, E., 2009. Exhumation of oceanic blueschists and eclogites in subduction zones: Timing and mechanisms. *Earth-Science Reviews*, 92, 53–79. <https://doi.org/10.1016/j.earscirev.2008.11.002>
- Agard, P., Yamato, P., Soret, M., Prigent, C., Guillot, S., Plunder, A., Dubacq, B., Chauvet, A., Monié, P., 2016. Plate interface rheological switches during subduction infancy: Control on slab penetration and metamorphic sole formation. *Earth and Planetary Science Letters*, 451, 208–220, <https://doi.org/10.1016/j.epsl.2016.06.054>
- Arcay, D., 2012. Dynamics of interplate domain in subduction zones: Influence of rheological parameters and subducting plate age. *Solid Earth*, 3(2), 467–488. <https://doi.org/10.5194/se-3-467-2012>
- Arcay, D., Tric, E., Doin, M.P., 2007. Slab surface temperature in subduction zones: Influence of the interplate decoupling depth and upper plate thinning processes. *Earth and Planetary Science Letters*, 255(3–4), 324–338. <https://doi.org/10.1016/j.epsl.2006.12.027>
- Arcay, D., 2017. Modelling the interplate domain in thermo-mechanical simulations of subduction: Critical effects of resolution and rheology, and consequences on wet mantle melting. *Physics of the Earth and Planetary Interiors*, 269, 112–132. <https://doi.org/10.1016/j.pepi.2017.05.008>
- Bangerth W., Dannberg, J., Gassmoeller, R., Heister., T., 2020a. ASPECT v2.1.0. (version v2.1.0). Zenodo. <https://doi.org/10.5281/ZENODO.3924604>.
- Bangerth, W., Dannberg, J., Gassmoeller, R., Heister, T., and others. 2020b. ASPECT: Advanced Solver for Problems in Earth's ConvecTion, User Manual. <https://doi.org/10.6084/m9.figshare.4865333>

- Beall, A., Fagereng, Å., Davies, J.H., Ga, F., Davies, D.R., 2020. Influence of Subduction Zone Dynamics on Interface Shear Stress and Potential Relationship with Seismogenic Behavior. *Geochemistry, Geophysics, Geosystems*, <https://doi.org/10.1029/2020GC009267>
- Bebout, G.E., Penniston-Dorland, S.C., 2016. Fluid and mass transfer at subduction interfaces-The field metamorphic record. *Lithos*, 240-243, 228-258, <https://doi.org/10.1016/j.lithos.2015.10.007>
- Becker, T.W., 2006. On the effect of temperature and strain-rate dependent viscosity on global mantle flow, net rotation, and plate-driving forces. *Geophysical Journal International*, 167(2), 943-957, <https://doi.org/10.1111/j.1365-246X.2006.03172.x>
- Behn, M.D., Kelemen, P.B., Hirth, G., Hacker, B.R., Massonne, H.J., 2011. Diapirs as the source of the sediment signature in arc lavas. *Nature Geoscience*, 4, 641-646, <https://doi.org/10.1038/ngeo1214>
- Behr, W.M., Becker, T.W., 2018. Sediment control on subduction plate speeds. *Earth and Planetary Science Letters*, 502, 166-173, <https://doi.org/10.1016/j.epsl.2018.08.057>
- Byerlee, J., 1978. Friction of rocks. *Pure and Applied Geophysics*, 116 (4-5), 615-626 <https://doi.org/10.1007/BF00876528>
- Cerpa, N.G., Hassani, R., Gerbault, M., Prévost, J.H., 2014. A fictitious domain method for lithosphere-asthenosphere interaction: Application to periodic slab folding in the upper mantle. *Geochemistry, Geophysics, Geosystems*, 15(5), 1852-1877, <https://doi.org/10.1002/2014GC005241>
- Clark, S.R., Stegman, D., Müller, R.D., 2008. Episodicity in back-arc tectonic regimes. *Physics of the Earth and Planetary Interiors*, 171(1-4), 265-279, <https://doi.org/10.1016/j.pepi.2008.04.012>
- Cloos, M., 1985. Thermal evolution of convergent plate margins: Thermal modeling and reevaluation of isotopic AR-ages for Blueschists in the Franciscan Complex of California. *Tectonics*, 4, 421-433, <https://doi.org/10.1029/TC004i005p00421>
- Condit, C. B., V. E. Guevara, J. R. Delph, French, M. E., 2020. Slab dehydration in warm subduction zones at depths of episodic slip and tremor, *Earth and Planetary Science Letters*, 552, <https://doi.org/10.1016/j.epsl.2020.116601>
- Connolly, J.A.D., Petrini, K., 2002. An automated strategy for calculation of phase diagram sections and retrieval of rock properties as a function of physical conditions. *Journal of Metamorphic Geology*, 20, 697-708, <https://doi.org/10.1046/j.1525-1314.2002.00398.x>
- Cottrell, E., Kelley, K.A., 2011. The oxidation state of Fe in MORB glasses and the oxygen fugacity of the upper mantle, *Earth and Planetary Science Letters*, 305(3-4), 270-282, doi:10.1016/j.epsl.2011.03.014.

- Cooper, L.B., Ruscitto, D.M., Plank, T., Wallace, P.J., Syracuse, E.M., Manning, C.E., 2012. Global variations in H<sub>2</sub>O/Ce: 1. Slab surface temperatures beneath volcanic arcs. *Geochemistry, Geophysics, Geosystems*, 13, 1-27 <https://doi.org/10.1029/2011GC003902>
- Currie, C.A., Wang, K., Hyndman, R.D., He, J., 2004. The thermal effects of steady-state slab-driven mantle flow above a subducting plate: The Cascadia subduction zone and backarc. *Earth and Planetary Science Letters*, 223(1-2), 35-48, <https://doi.org/10.1016/j.epsl.2004.04.020>
- Davies, D.R., Le Voci, G., Goes, S., Kramer, S.C., Wilson, C.R., 2016. The mantle wedge's transient 3-D flow regime and thermal structure. *Geochemistry, Geophysics, Geosystems*, 17(1), 78-100, <https://doi.org/10.1002/2015GC006125>
- Davies, J.H., 1999. Simple analytic model for subduction zone thermal structure. *Geophysical Journal International*, 139(3), 823-828, <https://doi.org/10.1046/j.1365-246x.1999.00991.x>
- Dymkova, D., Gerya, T., 2013. Porous fluid flow enables oceanic subduction initiation on Earth. *Geophysical Research Letters*, 40(21), 5671-5676, <https://doi.org/10.1002/2013GL057798>
- Eberle, M.A., Grasset, O., Sotin, C., 2002. A numerical study of the interaction between the mantle wedge, subducting slab, and overriding plate. *Physics of the Earth and Planetary Interiors*, 134(3-4), 191-202, [https://doi.org/10.1016/S0031-9201\(02\)00157-7](https://doi.org/10.1016/S0031-9201(02)00157-7)
- England, P.C., Katz, R.F., 2010. Melting above the anhydrous solidus controls the location of volcanic arcs. *Nature*, 467, 700-703, <https://doi.org/10.1038/nature09417>
- Enns, A., Becker, T.W., Schmeling, H., 2005. The dynamics of subduction and trench migration for viscosity stratification. *Geophysical Journal International*, 160, 761-775, <https://doi.org/10.1111/j.1365-246X.2005.02519.x>
- Faccenda, M. (2014), Water in the slab: A trilogy, *Tectonophysics*, 614, 1-30, doi:10.1016/j.tecto.2013.12.020.
- Faccenna, C., Becker, T.W., Lucente, F.P., Jolivet, L., Rossetti, F., 2001. History of subduction and back-arc extension in the central Mediterranean. *Geophysical Journal International*, 145(3), 809-820, <https://doi.org/10.1046/j.0956-540X.2001.01435.x>
- Funiciello, F., Faccenna, C., Heuret, A., Lallemand, S., Di Giuseppe, E., Becker, T.W., 2008. Trench migration, net rotation and slab-mantle coupling. *Earth and Planetary Science Letters*, 271(1-4), 233-240, <https://doi.org/10.1016/j.epsl.2008.04.006>
- Funiciello, F., Faccenna, C., Giardini, D., 2004. Role of lateral mantle flow in the evolution of subduction systems: Insights from laboratory experiments. *Geophysical Journal International*, 157(3), 1393-1406, <https://doi.org/10.1111/j.1365-246X.2004.02313.x>
- Furukawa, Y., 1993. Depth of the decoupling plate interface and thermal structure under arcs. *Journal of Geophysical Research*, 98, 20,005-20,013, <https://doi.org/10.1029/93jb02020>

- Gale, A., C. A. Dalton, C. H. Langmuir, Y. Su, Schilling, J.G., 2013. The mean composition of ocean ridge basalts, *Geochemistry, Geophysics, Geosystems*, 14(3), 489–518, doi:10.1029/2012GC004334.
- Gao, X., Wang, K., 2014. Strength of stick-slip and creeping subduction megathrusts from heat flow observations. *Science*, 345(6200), 1038-1041, <https://doi.org/10.1126/science.1255487>
- Garel, F., Goes, S., Davies, D.R., Davies, J.H., Kramer, S.C., Wilson, C.R., 2014. Interaction of subducted slabs with the mantle transition-zone: A regime diagram from 2-D thermo-mechanical models with a mobile trench and an overriding plate. *Geochemistry, Geophysics, Geosystems*, 15(5), 1739-1765.
- Gerya, T. V., Stöckhert, B., Perchuk, A.L., 2002. Exhumation of high-pressure metamorphic rocks in a subduction channel: A numerical simulation. *Tectonics*, 21(6), <https://doi.org/10.1029/2002tc001406>
- Gerya, T. V., Yuen, D.A., 2003. Rayleigh-Taylor instabilities from hydration and melting propel “cold plumes” at subduction zones. *Earth and Planetary Science Letters*, 212, 47–62. [https://doi.org/10.1016/S0012-821X\(03\)00265-6](https://doi.org/10.1016/S0012-821X(03)00265-6)
- Grevemeyer, I., Ranero, C.R., and Ivandic, M., 2018, Structure of oceanic crust and serpentinization at subduction trenches: *Geosphere*, 14, (2), 395–418, <https://doi.org/10.1130/GES01537.1>
- Groppo, C., Beltrando, M., Compagnoni, R., 2009. The P–T path of the ultra-high pressure Lago Di Cignana and adjoining high-pressure meta-ophiolitic units: insights into the evolution of the subducting Tethyan slab. *Journal of Metamorphic Geology*, 27(3), 207-231. <https://doi.org/10.1111/j.1525-1314.2009.00814.x>
- Grove, T.L., Till, C.B., Lev, E., Chatterjee, N., Médard, E., 2009. Kinematic variables and water transport control the formation and location of arc volcanoes. *Nature*, 459, 694-697, <https://doi.org/10.1038/nature08044>
- Grove, T.L., Till, C.B., Krawczynski, M.J., 2012. The role of H<sub>2</sub>O in subduction zone magmatism. *Annual Reviews of Earth and Planetary Sciences*, 40, 413-439, <https://doi.org/10.1146/annurev-earth-042711-105310>
- Guillot, S., Hattori, K., Agard, P., Schwartz, S., Vidal, O., 2009. Exhumation processes in oceanic and continental subduction contexts: A review. In S. Lallemand, & F. Funiciello (Eds.), *Subduction zone geodynamics, Frontiers in Earth Sciences* (pp. 175–205). Berlin, Germany: Springer.
- Hacker, B.R., 2008. H<sub>2</sub>O subduction beyond arcs. *Geochemistry, Geophysics, Geosystems*, 9, Q03001, <https://doi.org/10.1029/2007GC001707>
- Hacker, B. R., Peacock, S. M., Abers, G. A., and Holloway, S. D. (2003), Subduction factory 2. Are intermediate-depth earthquakes in subducting slabs linked to metamorphic dehydration

- reactions? *Journal of Geophysical Research.*, 108, 2030,  
<https://doi.org/10.1029/2001JB001129>,
- Hager, B.H., 1984. Subducted slabs and the geoid: constraints on mantle rheology and flow. *Journal of Geophysical Research*, 89, 6003-6015,  
<https://doi.org/10.1029/JB089iB07p06003>
- Hall, P.S., 2012. On the thermal evolution of the mantle wedge at subduction zones. *Physics of the Earth and Planetary Interiors*, 198–199, 9–27.  
<https://doi.org/10.1016/j.pepi.2012.03.004>
- Heister, T., Dannberg, J., Gassmüller, R., Bangerth, W., 2017. High accuracy mantle convection simulation through modern numerical methods - II: Realistic models and problems. *Geophysical Journal International*, 210(2), 833-851, <https://doi.org/10.1093/gji/ggx195>
- Hernández-Uribe, D., Palin, R.M., 2019. A revised petrological model for subducted oceanic crust: Insights from phase equilibrium modelling. *Journal of Metamorphic Geology*, 37, 745–768. <https://doi.org/10.1111/jmg.12483>
- Hernández-Uribe, D., Palin, R.M., Cone, K.A., Cao, W., 2020. Petrological implications of seafloor hydrothermal alteration of subducted mid-ocean ridge basalt. *Journal of Petrology*, 61(9), doi:10.1093/petrology/egaa086
- Hirauchi, K., Katayama, I., 2013. Rheological contrast between serpentine species and implications for slab-mantle wedge decoupling. *Tectonophysics*, 608, 545–551.  
<https://doi.org/10.1016/j.tecto.2013.08.027>
- Hirth, G., Kohlstedt, D.L., 2003. Rheology of the Upper Mantle and the Mantle Wedge: a View From the Experimentalists. In *Inside the Subduction Factory, Geophysical Monograph Series* 138, 83-106, American Geophysical Union, Washington, D.C.
- Holland, T., Powell, R., 1991. A Compensated-Redlich-Kwong (CORK) equation for volumes and fugacities of CO<sub>2</sub> and H<sub>2</sub>O in the range 1 bar to 50 kbar and 100-1600°C, *Contributions to Mineralogy and Petrology*, 109(2), 265–273, doi:10.1007/BF00306484.
- Holland, T., Powell, R., 1998. An internally consistent thermodynamic data set for phases of petrological interest, *Journal of Metamorphic Geology*, 16, 309–343, doi:10.1111/J.1525-1314.1998.00140.X
- Holland, T., Powell, R., 2011. An improved and extended internally consistent thermodynamic dataset for phases of petrological interest, involving a new equation of state for solids, *Journal of Metamorphic Geology*, 29(3), 333–383, doi:10.1111/j.1525-1314.2010.00923.x.
- Holt, A.F., Becker, T.W., Buffett, B.A., 2015. Trench migration and overriding plate stress in dynamic subduction models. *Geophysical Journal International*, 201, 172–192.  
<https://doi.org/10.1093/gji/ggv011>

- Holt, A.F., Becker, T.W., 2017. The effect of a power-law mantle viscosity on trench retreat rate. *Geophysical Journal International*, 208, 491-507, <https://doi.org/10.1093/gji/ggw392>
- Holt, A. F., Royden, L. H., Becker, T. W., 2017. The dynamics of double slab subduction. *Geophysical Journal International*, 209, 250-265, doi:10.1093/gji/ggw496.
- Honda, S., 1985. Thermal structure beneath Tohoku, northeast Japan. *Tectonophysics*. 112(1-4), 69-102, [https://doi.org/10.1016/0040-1951\(85\)90173-8](https://doi.org/10.1016/0040-1951(85)90173-8)
- Honda, S., Saito, M., 2003. Small-scale convection under the back-arc occurring in the low viscosity wedge. *Earth and Planetary Science Letters*, 216(4), 703-715, [https://doi.org/10.1016/S0012-821X\(03\)00537-5](https://doi.org/10.1016/S0012-821X(03)00537-5)
- Iaffaldano, G., Bunge, H.P., 2015. Rapid plate motion variations through geological time: Observations serving geodynamic interpretation. *Annual Reviews of Earth and Planetary Sciences*, 43, 571-592, <https://doi.org/10.1146/annurev-earth-060614-105117>
- Jarrard, R. D. (2003), Subduction fluxes of water, carbon dioxide, chlorine, and potassium, *Geochemistry, Geophysics, Geosystems*, 4, 8905, doi:[10.1029/2002GC000392](https://doi.org/10.1029/2002GC000392)
- Karato, S.I., Wu, P., 1993. Rheology of the upper mantle: A synthesis. *Science*, 260, 771-778, <https://doi.org/10.1126/science.260.5109.771>
- Kelemen, P.B., Rilling, J.L., Parmentier, E.M., Mehl, L., Hacker, B.R., 2004. Thermal structure due to solid-state flow in the mantle wedge beneath arcs. In *Inside the Subduction Factory, Geophysical Monograph Series* 138, 293–311, American Geophysical Union, Washington, D.C.
- Kincaid, C., Griffiths, R.W., 2003. Laboratory models of the thermal evolution of the mantle during rollback subduction. *Nature*, 425, 58-62, <https://doi.org/10.1038/nature01923>
- Kincaid, C., Sacks, I.S., 1997. Thermal and dynamical evolution of the upper mantle in subduction zones. *Journal of Geophysical Research Solid Earth*, 102, 12295–12315. <https://doi.org/10.1029/96jb03553>
- King, S.D., Ita, J.J., 2005. Subduction and volatile recycling in earth's mantle. AIP Conference Proceedings, 341, 33–44. <https://doi.org/10.1063/1.48748>
- Kirby, S., Engdahl, E.R., Denlinger, R., 1996. Intermediate-depth intraslab earthquakes and arc volcanism as physical expressions of crustal and uppermost mantle metamorphism in subducting slabs. In *Subduction Topo to Bottom, Geophysical Monograph Series* 96, 195-214, American Geophysical Union, Washington, D.C.
- Korenaga, J., 2017. On the extent of mantle hydration caused by plate bending. *Earth and Planetary Science Letters*, 457, 1–9, doi:10.1016/j.epsl.2016.10.011



- Krebs, M., Schertl, H.-P., Maresch, W.V., Draper, G. Mass flow in serpentinite-hosted subduction channels: P–T–t path patterns of metamorphic blocks in the Rio San Juan mélange (Dominican Republic). *Journal of Asian Earth Sciences*, 42(4), 569–595, <https://doi.org/10.1016/j.jseaes.2011.01.011>.
- Kronbichler, M., Heister, T., Bangerth, W., 2012. High accuracy mantle convection simulation through modern numerical methods. *Geophysical Journal International*, 191(1), 12–29, <https://doi.org/10.1111/j.1365-246X.2012.05609.x>
- Lázaro, C., García-Casco, A., Agramonte Y.R., Kröner A., Neubauer F., Iturralde-Vinent, M.A., 2009. Fifty-five-million-year history of oceanic subduction and exhumation at the northern edge of the Caribbean plate (Sierra del Convento melange, Cuba), *Journal of Metamorphic Geology*, 27, 19–40
- Matsumoto, T., Tomoda, Y., 1983. Numerical simulation of the initiation of subduction at the fracture zone. *Journal of Physics of the Earth*, 31, 183–194. <https://doi.org/10.4294/jpe1952.31.183>
- Maunder, B., Goes, S., van Hunen, J., Prytulak, J., P., Magni, V., Bouilhol, P., 2018. The Decoupling Depth and Slab Thermal Structure. Abstract DI23B-0030 presented at 2018 Fall Meeting, American Geophysical Union, Washington, D.C., 10–14 Dec.
- Maunder, B., van Hunen, J., Bouilhol, P., Magni, V., 2019. Modeling Slab Temperature: A Reevaluation of the Thermal Parameter. *Geochemistry, Geophys. Geosystems*. 20, 673–687. <https://doi.org/10.1029/2018GC007641>
- McKenzie, D.P., 1969. Speculations on the Consequences and Causes of Plate Motions. *Geophysical Journal of the Royal Astronomical Society*, 18, 1, <https://doi.org/10.1111/j.1365-246X.1969.tb00259.x>
- Miyashiro, A., F. Shido, Ewing, E., 1969. Composition and origin of serpentinites from the Mid-Atlantic Ridge near 24° and 30° North Latitude, *Contributions to Mineralogy and Petrology*, 23(2), 117–127, doi:10.1007/BF00375173.
- Miyazaki, K., Ozaki, M., Saito, M., Toshimitsu, S., 2016. The Kyushu–Ryukyu Arc, in: The Geology of Japan. <https://doi.org/10.1144/goj>.
- Molnar, P., England, P., 1990. Temperatures, heat flux, and frictional stress near major thrust faults. *Journal of Geophysical Research*, 95(B4), 4833–4856. <https://doi.org/10.1029/JB095iB04p04833>
- Molnar, P., England, P., 1995. Temperatures in zones of steady-state underthrusting of young oceanic lithosphere. *Earth and Planetary Science Letters*, 131(1–2), 57–70. [https://doi.org/10.1016/0012-821X\(94\)00253-U](https://doi.org/10.1016/0012-821X(94)00253-U)
- Sdrolias, M., Müller, R.D., 2006. Controls on back-arc basin formation. *Geochemistry, Geophysics, Geosystems*, 7(4), <https://doi.org/10.1029/2005GC001090>.

- Naif, S., K. Key, S. Constable, Evans, R. L., 2015. Water-rich bending faults and the Middle America Trench. *Geochemistry Geophysics, Geosystems*, 16(1), 267–300, doi:10.1002/2014GC005684.Key.
- Peacock, S.M., 1991. Numerical simulation of subduction zone pressure-temperature-time paths: constraints on fluid production and arc magmatism. *Philosophical Transactions of the Royal Society A*, 335(1638), 341–353. <https://doi.org/10.1098/rsta.1991.0050>
- Peacock, S.M., 1992. Blueschist-facies metamorphism, shear heating, and P-T-t paths in subduction shear zones. *Journal of Geophysical Research: Solid Earth*, 97(B12), 17963–17707, <https://doi.org/10.1029/92JB01768>
- Peacock, S. M., 2001. Are the lower planes of double seismic zones caused by serpentine dehydration in subducting oceanic mantle? *Geology*, 29(4), 299–302, doi:10.1130/0091-7613
- Peacock, S.M., 2020. Advances in the thermal and petrologic modeling of subduction zones. *Geosphere*, 16(4), 936-952. <https://doi.org/10.1130/GES02213.1>
- Peacock, S.M., Wang, K., 1999. Seismic consequences of warm versus cool subduction metamorphism: Examples from southwest and northeast Japan. *Science*, 286(5441), 937–939. <https://doi.org/10.1126/science.286.5441.937>
- Peacock, S.M., Wang, K., 2020. Does the stability of talc in the mantle wedge control the maximum depth of slab-wedge decoupling in subduction zones? Abstract T052-02 presented at 2020 Fall Meeting, American Geophysical Union, Virtual, 1-17 Dec.
- Penniston-Dorland, S.C., Kohn, M.J., Manning, C.E., 2015. The global range of subduction zone thermal structures from exhumed blueschists and eclogites: Rocks are hotter than models. *Earth and Planetary Science Letters*, 428, 243–254. <https://doi.org/10.1016/j.epsl.2015.07.031>
- Perrin, A., Goes, S., Prytulak, J., Rondenay, S., Davies, D.R., 2018. Mantle wedge temperatures and their potential relation to volcanic arc location. *Earth and Planetary Science Letters*, 501, 67–77. <https://doi.org/10.1016/j.epsl.2018.08.011>
- Platt, J.P., 1975. Metamorphic and deformational processes in the Franciscan Complex, California: Some insights from the Catalina Schist terrane. *GSA Bulletin*, 86(10), 1337-1347, [https://doi.org/10.1130/0016-7606\(1975\)86<1337:MADPIT>2.0.CO;2](https://doi.org/10.1130/0016-7606(1975)86<1337:MADPIT>2.0.CO;2)
- Plunder, A., Thieulot, C., van Hinsbergen, D.J.J., 2018. The effect of obliquity on temperature in subduction zones: insights from 3-D numerical modeling. *Solid Earth*, 9, 759–776. <https://doi.org/10.5194/se-9-759-2018>
- Podolefsky, N.S., Zhong, S., McNamara, A.K., 2004. The anisotropic and rheological structure of the oceanic upper mantle from a simple model of plate shear. *Geophysical Journal International*, 158(1), 287-296, <https://doi.org/10.1111/j.1365-246X.2004.02250.x>

- Prigent, C., Warren, J.M., Kohli, A.H., Teyssier, C., 2020. Fracture-mediated deep seawater flow and mantle hydration on oceanic transform faults. *Earth and Planetary Science Letters*, 535, <https://doi.org/10.1016/j.epsl.2019.115988>
- Rotman, H.M.M., Spinelli, G.A., 2013. Global analysis of the effect of fluid flow on subduction zone temperatures. *Geochemistry, Geophysics, Geosystems*, 14(8), 3268-3281, <https://doi.org/10.1002/ggge.20205>
- Royden, L.H., 1993. The steady state thermal structure of eroding orogenic belts and accretionary prisms. *Journal of Geophysical Research*, 98(B3), 4487-4507, <https://doi.org/10.1029/92JB01954>
- Ruh, J.B., Pourhiet, L.L., Agard, P., Burov, E.B., Gerya, T., 2015. Tectonic slicing of subducting oceanic crust along plate interfaces: Numerical modeling. *Geochemistry, Geophysics, Geosystems*, 16, 3505–3531, doi:10.1002/2015GC005998.
- Rüpke, L.H., Morgan, J.P., Hort, M., Connolly, J.A.D., 2004. Serpentine and the subduction zone water cycle. *Earth and Planetary Science Letters*, 223(1-2), 17-34, <https://doi.org/10.1016/j.epsl.2004.04.018>
- Sandiford, D., Moresi, L., 2019. Improving subduction interface implementation in dynamic numerical models. *Solid Earth*, 10, 969-985, <https://doi.org/10.5194/se-10-969-2019>
- Schmidt, M. W., Poli, S., 1998. Experimentally based water budgets for dehydrating slabs and consequences for arc magma generation. *Earth and Planetary Science Letters*, 163, 361–379, [https://doi.org/10.1016/S0012-821X\(98\)00142-3](https://doi.org/10.1016/S0012-821X(98)00142-3)
- Sdrolias, M., Müller, R.D., 2006. Controls on back-arc basin formation. *Geochemistry, Geophysics, Geosystems*, 7(4), Q04016, <https://doi.org/10.1029/2005GC001090>
- Stein, C.A., Stein, S., 1992. A model for the global variation in oceanic depth and heat flow with lithospheric age. *Nature*, 359, 123-129, <https://doi.org/10.1038/359123a0>
- Suenaga, N., Yoshioka, S., Matsumoto, T., Manea, V. C., Manea, M., & Ji, Y. (2019). Two-dimensional thermal modeling of the Philippine Sea plate subduction in central Japan: Implications for gap of low-frequency earthquakes and tectonic tremors. *Journal of Geophysical Research: Solid Earth*, 124, 6848–6865. <https://doi.org/10.1029/2018JB017068>
- Syracuse, E.M., van Keken, P.E., Abers, G.A., 2010. The global range of subduction zone thermal models. *Physics of the Earth and Planetary Interiors*, 183, 73–90. <https://doi.org/10.1016/j.pepi.2010.02.004>
- Tanaka, A., Yamano, M., Yano, Y., Sasada, M., 2004. Geothermal gradient and heat flow data in and around Japan (I): Appraisal of heat flow from geothermal gradient data. *Earth, Planets and Space*, 56, 1191-1194, <https://doi.org/10.1186/BF03353339>

- Tatsumi, Y., 1986. Formation of the volcanic front in subduction zones. *Geophysical Research Letters*, 13, 717-720, <https://doi.org/10.1029/GL013i008p00717>
- van Keken, P.E., Hacker, B.R., Syracuse, E.M., Abers, G.A., 2011. Subduction factory: 4. Depth-dependent flux of H<sub>2</sub>O from subducting slabs worldwide. *Journal of Geophysical Research Solid Earth*, 116, B01401, <https://doi.org/10.1029/2010JB007922>
- van Keken, P.E., Kiefer, B., Peacock, S.M., 2002. High-resolution models of subduction zones: Implications for mineral dehydration reactions and the transport of water into the deep mantle. *Geochemistry, Geophysics, Geosystems*, 3(10), 1056, <https://doi.org/10.1029/2001GC000256>
- van Keken, P.E., Wada, I., Abers, G.A., Hacker, B.R., Wang, K., 2018. Mafic High-Pressure Rocks Are Preferentially Exhumed From Warm Subduction Settings. *Geochemistry, Geophysics, Geosystems*, 19, 2934–2961. <https://doi.org/10.1029/2018GC007624>
- Wada, I., Wang, K., 2009. Common depth of slab-mantle decoupling: Reconciling diversity and uniformity of subduction zones. *Geochemistry, Geophysics, Geosystems*, 10(10), 2009Q10009, <https://doi.org/10.1029/2009GC002570>
- Wada, I., Wang, K., He, J., Hyndman, R.D., 2008. Weakening of the subduction interface and its effects on surface heat flow, slab dehydration, and mantle wedge serpentinization. *Journal of Geophysical Research Solid Earth*, 113(B4), B04402, <https://doi.org/10.1029/2007JB005190>
- Wada, I., Rychert, C.A., Wang, K., 2011. Sharp thermal transition in the forearc mantle as a consequence of nonlinear mantle wedge flow. *Geophysical Research Letters*, 38(13), <https://doi.org/10.1029/2011GL047705>
- Wu, B., Conrad, C.P., Heuret, A., Lithgow-Bertelloni, C., Lallemand, S., 2008. Reconciling strong slab pull and weak plate bending: The plate motion constraint on the strength of mantle slabs. *Earth and Planetary Science Letters*, 272(1-2), 412-421, <https://doi.org/10.1016/j.epsl.2008.05.009>
- Wu, J.T.J., Wu, J., 2019. Izanagi-Pacific ridge subduction revealed by a 56 to 46 Ma magmatic gap along the northeast Asian margin. *Geology*, 47(10), 953-957, <https://doi.org/10.1130/G46778.1>
- Yamato, P., Agard, P., Burov, E., Le Pourhiet, L., Jolivet, L., Tiberi, C., 2007. Burial and exhumation in a subduction wedge: Mutual constraints from thermomechanical modeling and natural P-T-t data (Schistes Lustrés, western Alps). *Journal of Geophysical Research Solid Earth*, 112, B07410, <https://doi.org/10.1029/2006JB004441>

Quantity	Symbol	Units	Value
Thermal expansion coefficient	$\alpha$	$\text{K}^{-1}$	$3 \times 10^{-5}$
Thermal diffusivity	$\kappa$	$\text{m}^2 \text{s}^{-1}$	$10^{-6}$
Reference density	$\rho_0$	$\text{kg m}^{-3}$	3300
Surface temperature	$T_s$	K	273
Potential temperature	$T_m$	K	1694.5
Adiabatic temperature gradient	$d_z T$	$\text{K km}^{-1}$	0.3
Gravitational acceleration	$g$	$\text{m s}^{-2}$	9.81
Maximum viscosity	$\eta_{max}$	Pa s	$2.5 \times 10^{23}$
Minimum viscosity	$\eta_{min}$	Pa s	$2.5 \times 10^{18}$
Crust viscosity	$\eta_C$	Pa s	$2.0 \times 10^{20}$
Core viscosity	$\eta_{core}$	Pa s	$2.5 \times 10^{23}$
<b>Dislocation creep (upper mantle)</b>			
Activation energy	$E$	$\text{kJ mol}^{-1}$	540
Activation volume	$V$	$\text{cm}^3 \text{mol}^{-1}$	12
Prefactor	$A$	$\text{Pa}^{-n} \text{s}^{-1}$	$3.275 \times 10^{-16}$
Exponent	$n$	-	3.5
<b>Diffusion creep (upper and lower mantle)</b>			
Activation energy	$E$	$\text{kJ mol}^{-1}$	300 (UM & LM)
Activation volume	$V$	$\text{cm}^3 \text{mol}^{-1}$	4 (UM), 2.5 (LM)
Prefactor	$A$	$\text{Pa}^{-1} \text{s}^{-1}$	$1.92 \times 10^{-11}$ (UM)
			$1.67 \times 10^{-13}$ (LM)
Exponent	$n$	-	1
<b>Byerlee yielding</b>			
Cohesion	$b$	MPa	60
Friction coefficient	$a$	-	0.6
Pre-factor	$\lambda$	-	0.1
Maximum yield stress	$\tau_{max}$	MPa	500

**Table 1:** Basic reference model parameters.